Numerical Simulations and a Conceptual Model of the Stratocumulus to Trade Cumulus Transition

MATTHEW C. WYANT AND CHRISTOPHER S. BRETHERTON

Department of Atmospheric Sciences, University of Washington, Seattle, Washington

HUGH A. RAND

Department of Applied Mathematics, University of Washington, Seattle, Washington

DAVID E. STEVENS

Courant Institute of Mathematical Sciences, New York, New York

(Manuscript received 8 November 1995, in final form 26 June 1996)

ABSTRACT

A two-dimensional eddy-resolving model is used to study the transition from the stratocumulus topped boundary layer to the trade cumulus boundary layer. The 10-day simulations use an idealized Lagrangian trajectory representative of summertime climatological conditions in the subtropical northeastern Pacific. The sea surface temperature is increased steadily at 1.5 K day^{-1}, reflecting the southwestward advection of the subtropical marine boundary layer by the trade winds, while the free tropospheric temperature remains unchanged. Results from simulations with both a fixed diurnally averaged shortwave radiative forcing and a diurnally varying shortwave forcing are presented.

A two-stage model for the boundary layer evolution consistent with these simulations is proposed. In the first stage, decoupling is induced by increased latent heat fluxes in the deepening boundary layer. After decoupling, cloud cover remains high, but the cloudiness regime changes from a single stratocumulus layer to sporadic cumulus that detrain into stratocumulus clouds. In the second stage, farther SST increase causes the cumuli to become deeper and more vigorous, penetrating farther into the inversion and entraining more and more dry above-inversion air. This evaporates liquid water in cumulus updrafts before they detrain, causing the eventual dissipation of the overlying stratocumulus. Diurnal variations of insolation lead to a large daytime reduction in stratocumulus cloud amount, but they have little impact on the systematic evolution of boundary layer structure and cloud. The simulated cloudiness changes are not consistent with existing criteria for cloud-top entrainment instability.

1. Introduction

Cloudiness in the marine boundary layer (MBL) has a substantial feedback on climate (Hartmann et al. 1992). The presence of clouds and associated convection in the MBL also has a large effect on the vertical structure of the MBL and air–sea fluxes of heat, moisture, and momentum (Tiedtke et al. 1988). Nevertheless, the complex interplay between radiation, convection, surface fluxes, and microphysics that determines the cloud fractional coverage and radiative properties in the MBL is still not well understood.

Subtropical MBL clouds off the west coasts of the major continents have been a particular focus of study for two main reasons. First, while their areal coverage is not as large as that of midlatitude MBL clouds (Klein and Hartmann 1993), they form in a synoptically steady environment characterized by equatorward advection of air toward warmer water and lower mean subsidence. Hence, a coherent phenomenology of MBL cloud cover can be synthesized from local observations from field programs such as the FIRE (First International Satellite Cloud Climatology Project Regional Experiment) Marine Stratocumulus Experiment (Albrecht et al. 1988) and ASTEX (the Atlantic Stratocumulus Transition Experiment; Albrecht et al. 1995); climatological information (Riehl et al. 1951; Neiburger et al. 1961; Klein and Hartmann 1993); and weathership data (Klein et al. 1995). Second, there is a prominent cloudiness transition, the stratocumulus to trade cumulus transition (STCT), which occurs as air from within the subtropical stratocumulus regime advects over the warmer water downwind. This is accompanied by a deepening and

Corresponding author address: Matthew C. Wyant, Department of Atmospheric Sciences, Box 351640, University of Washington, Seattle, WA 98195-1640.
E-mail: wyant@atmos.washington-edu

decoupling of the boundary layer, the development of trade cumulus clouds beneath the stratocumulus, and the gradual dissipation of the overlying stratocumulus (Albrecht et al. 1995; Klein et al. 1995), typically over a period of several days. By understanding this transition, we hope to gain more general insight into how to parameterize the interaction between cloudiness and MBL dynamics. The purpose of this paper is to present numerical simulations of the STCT and to show how they support a conceptual model of the STCT originally proposed by Bretherton (1992).

Simple mixed layer and more complex bulk models have provided considerable insight into both shallow stratocumulus-capped MBLs (Lilly 1968) and trade cumulus boundary layers (Albrecht et al. 1979). A simplified model that addressed the dynamics associated with the STCT was proposed by Wang (1993). In this model, both decoupling and the cumulus cloud properties were sensitively tied to internal parameters that had to be determined in an ad hoc way (Bretherton 1993). While the model produced an STCT, it did not provide clear insight into the underlying mechanisms.

Two- and three-dimensional numerical eddy-resolving models (ERMs) have become a useful tool for studying the MBL. Here the term ERM is used as a generalization of large-eddy simulation (LES), since the latter term is usually applied only to three-dimensional simulations. ERM studies of shallow nocturnal stratocumulus have achieved very realistic dynamics (Moeng 1986). Other ERM studies have focused on entrainment (e.g., Deardorff 1980; Kuo and Schubert 1988; Siems and Bretherton 1992; MacVean 1993; Moeng et al. 1995), roll and mesoscale structure (e.g., Sykes et al. 1988; Mason and Sykes 1982; Rand 1995), and explicit representation of the droplet and aerosol microphysics (Kogan et al. 1995; Stevens et al. 1996). ERM simulations of trade cumulus cloud fields in both two and three dimensions [e.g., Sommeria 1976; Soong and Ogura 1980; Krueger and Bergeron 1994; Siebesma and Cuijpers 1995] have examined turbulent transports and cloud properties and also have compared well with observations.

Using a ''Lagrangian'' approach (Wakefield and Schubert 1981; Bretherton and Pincus 1995), it is attractive to simulate the STCT using an ERM. In this approach, the air motions are computed within a column of air a few kilometers on a side that is moving with the mean MBL wind. As it moves, the column is subject to changing sea surface temperature (SST), free tropospheric temperature and mixing ratio, mean subsidence rate, and local horizontal pressure gradients. These time-varying boundary conditions cause the boundary layer characteristics within the column to evolve. Since the STCT takes several days, this type of simulation is computationally reasonable only for a two-dimensional domain at present.

The STCT can be isolated in a simple ''Lagrangian'' context possible by assuming free tropospheric conditions, subsidence, and geostrophic wind remain fixed while SST rises following the air column. Krueger et al. (1995a) performed such a simulation using a 5-km-wide by 3-km-high domain with 50-m resolution, with SST increasing by 1.8 K day^{-1} for 6 days. They obtained an STCT with accompanying changes in MBL depth and structure that were in good agreement with existing observations. Their simulations clearly showed the stages of evolution from a shallow well-mixed stratocumulus capped MBL to a deeper decoupled MBL with cumulus rising into stratocumulus (abbreviated in the rest of this paper as CuSc), followed by the dissipation of the overlying stratocumulus to leave behind a trade cumulus cloud field.

In this paper, we extend their study to present and justify a conceptual model of this sequence of events. We will particularly concern ourselves with (a) why the mixed layer decouples as SST rises, a process we call deepening-warming decoupling, and (b) why the stratocumulus that overlie the cumulus become thinner and dissipate as the boundary layer further deepens. Our analysis of deepening-warming decoupling is closely tied to the analysis in a companion paper (Bretherton and Wyant 1997, hereafter BW97) in which a mixed-layer model of the MBL is run with the same environmental conditions and rising SST as are used here. That paper derives a criterion for decoupling that is tested against our ERM results. We modify Krueger et al.'s (1995a) environmental conditions so that an air column experiences the summertime climatological conditions representative of Ocean Weather Station N at 30°N, 140°W five days into the simulation.

In section 2, we describe our ERM, and in section 3 we define the model initialization and cloudiness statistics we use. Section 4 presents an ERM simulation of the STCT similar to Krueger et al. (1995a). In our ''base'' simulation, the solar zenith angle is fixed so as to provide the same insolation as the average over the diurnal cycle and with observations. This is compared with a simulation incorporating the diurnal cycle of insolation. Section 5 reviews the conceptual model of the STCT (Bretherton 1992). Section 6 compares key predictions of the conceptual model with our numerical simulations. Section 7 presents sensitivity studies to domain size and initialization. Section 8 presents the conclusions.

2. Model description

a. Dynamical framework

Our numerical model, HUSCI, uses the anelastic momentum equations of Ogura and Phillips (1962). The base-state anelastic potential temperature $\bar{\theta}$ is constant with height. From this and the assumed surface pressure (p_0 = 1021 mb), a base-state density profile, $\bar{\rho}(z)$, is constructed assuming hydrostatic balance. The initial sounding is used to define ''environmental'' profiles

$\theta_{env}(z)$, temperature $T_{env}(z)$, and the hydrostatic pressure, $p_{env}(z)$. The pressure gradient terms in the anelastic equations are written in terms of the perturbation Exner function

$$\Pi' = \left(\frac{p}{1000\text{mb}}\right)^{R_d/C_p} - \Pi_{env}, \tag{1}$$

where $\Pi_{env} = T_{env}/\theta_{env}$, p is the pressure, R_d is the gas constant for dry air, and C_p is the specific heat of dry air at constant pressure. Water is partitioned into three categories: the cloud liquid water mixing ratio q_l, the rainwater mixing ratio q_r, and the water vapor mixing ratio q_v. Here cloud liquid water is defined to be suspended water droplets, while rainwater is allowed to gravitationally settle. The total water mixing ratio is defined as $q_t = q_v + q_l$. The liquid water potential temperature θ_l is defined in its linearized form as

$$\theta_l \equiv \theta - \frac{1}{\Pi_{env}}\frac{L}{C_p}q_l \tag{2}$$

and is approximately conserved during reversible adiabatic processes (L is the latent heat of vaporization).

The scalar prognostic variables that are advected by the model are θ_l, q_t, and q_r. Also computed each time step at each grid point are q_l, q_v, θ, T, and $\theta_v = \theta(1 + 0.61q_v - q_l)$. In computing these scalars, it is assumed that when q_l is nonzero, the air is exactly saturated with water vapor. The Clausius–Clapeyron equation used is given in section b of the appendix. Note that our definition of θ_v does not include rainwater loading. The simulated rainwater contents are at most 0.05 g kg^{-1}, so the maximum error in θ_v due to the neglect of rainwater loading is about 0.02 K. Future versions of HUSCI will include rainwater loading.

The model momentum and continuity equations are

$$\frac{D\mathbf{u}}{Dt} = -C_p\bar{\theta}\boldsymbol{\nabla}\Pi' + g\left(\frac{\theta_v - \bar{\theta}}{\bar{\theta}}\right)\mathbf{k} - f\mathbf{k}\times(\mathbf{u} - \mathbf{u}_g) + \frac{1}{\bar{\rho}}\boldsymbol{\nabla}\cdot(\bar{\rho}K_M\mathbf{D}) + \left(\frac{\partial\mathbf{u}}{\partial t}\right)_{\text{surface}}, \tag{3}$$

$$\boldsymbol{\nabla}\cdot(\bar{\rho}\mathbf{u}) = 0. \tag{4}$$

Here, f is the Coriolis parameter, $\mathbf{u}_g(z, t)$ is the geostrophic wind in the moving coordinate system, K_M is the turbulent eddy-viscosity, $\mathbf{D}$ is the deformation tensor, and the last term represents the surface drag, discussed later. The three scalar equations for θ_l, q_t, and q_r are

$$\frac{D\theta_l}{Dt} = -\frac{1}{\bar{\rho}C_p\Pi_{env}}\frac{\partial F_R}{\partial z} + \frac{1}{\bar{\rho}}\boldsymbol{\nabla}\cdot\bar{\rho}K_H\boldsymbol{\nabla}\theta_l + \left(\frac{\partial\theta_l}{\partial t}\right)_{\text{surface}} + \left(\frac{\partial\theta_l}{\partial t}\right)_{\text{microphysics}} + \left(\frac{\partial\theta_l}{\partial t}\right)_{\text{subsidence}}, \tag{5}$$

$$\frac{Dq_t}{Dt} = \frac{1}{\bar{\rho}}\boldsymbol{\nabla}\cdot\bar{\rho}K_Q\boldsymbol{\nabla}q_t + \left(\frac{\partial q_t}{\partial t}\right)_{\text{surface}} + \left(\frac{\partial q_t}{\partial t}\right)_{\text{microphysics}} + \left(\frac{\partial q_t}{\partial t}\right)_{\text{subsidence}}, \tag{6}$$

$$\frac{Dq_r}{Dt} = \frac{1}{\bar{\rho}}\boldsymbol{\nabla}\cdot\bar{\rho}K_Q\boldsymbol{\nabla}q_r + \left(\frac{\partial q_r}{\partial t}\right)_{\text{microphysics}}, \tag{7}$$

where F_R is the net upward radiative flux, K_H and K_Q are the turbulent eddy viscosities for heat and moisture, and the operator $D/Dt = \partial/\partial t + \mathbf{u}\cdot\boldsymbol{\nabla}$. The partial time-derivative terms represent the parameterized effects of the surface fluxes, microphysics, and large-scale subsidence. The appendix describes the microphysics, turbulence, and radiation parameterizations, and the numerical methods used in the model. Above the inversion, there are additional sources $(d\theta_l/dt)_{\text{relaxation}}$, $(dq/dt)_{\text{relaxation}}$, and $(d\mathbf{u}/dt)_{\text{sponge}}$, described below. For numerical stability, the model is formulated with respect to a moving reference frame translating with an arbitrary ground-relative velocity (U, V, 0).

b. Boundary conditions

Rigid-lid boundary conditions ($w = 0$) are applied at the top and bottom of the model domain. For the horizontal velocities at the bottom of the domain we specify a relation between the velocity at the lowest grid points and the surface stress. At the top of the domain, we use stress-free boundary conditions for the horizontal velocities. Periodic horizontal boundary conditions are applied for all scalar and momentum variables.

For the simulations presented here, we assume that the geostrophic wind is uniform with height and we choose the translation velocity of our coordinate system to be equal to the geostrophic wind, so that in the translating reference frame $\mathbf{u}_g = 0$. In this case, the base state is geostrophically balanced and independent of horizontal position, which simplifies the implementation of periodic horizontal boundary conditions at the sides of the domain.

The horizontal large-scale U velocity components in these simulations are $U = 5.0$ m s^{-1} and $V = -5.0$ m s^{-1}. In the model reference frame, this is equivalent to a sea surface velocity of 5.0 m s^{-1} to the left and 5.0 m s^{-1} into the x–z plane of the simulation. The choice of angle of domain x–z plane orientation to domain translation is rather arbitrary but not critical to the results.

c. Surface fluxes

The model surface fluxes are computed using bulk thermodynamic formulas appropriate for a neutrally stable or convectively unstable boundary layer. The surface fluxes of θ_l and q_t are

$$(\overline{w'\theta_l'})_0 = -C_H|\mathbf{V}_0|(T_0 - \mathrm{SST}),$$
$$(\overline{w'q_t'})_0 = -C_Q|\mathbf{V}_0|(q_t0 - q_{\mathrm{sat}}(p_0, \mathrm{SST})),$$
$$|\mathbf{V}_0| = \sqrt{(U + u_0)^2 + (V + v_0)^2}, \quad (8)$$

where C_H and C_Q are bulk transfer coefficients and q_{t0}, T_0, u_0, and v_0 are taken from the lowest grid point of the model domain, at 12.5-m height in the simulations presented here. Similarly the surface momentum fluxes are given by

$$(\overline{u'w'})_0 = -C_D|\mathbf{V}_0|(U + u_0)$$
$$(\overline{v'w'})_0 = -C_D|\mathbf{V}_0|(V + v_0), \quad (9)$$

where C_D is the bulk momentum transfer coefficient. We set $C_D = C_H = C_Q = 0.0014$.

To ensure efficient vertical transfer of surface fluxes, the model sources of momentum and scalar quantities due to surface fluxes are distributed vertically over the bottom three grid points. At a given horizontal grid position, 50% of the total source goes into the lowest grid point, 30% to the second lowest, and 20% to the third lowest.

d. Large-scale subsidence

The large-scale subsidence is specified in a way similar to that of Sommeria (1976) and Schubert et al. (1979). In the boundary layer the subsidence velocity is given by $W = -Dz$, where D is the large-scale divergence. Above the inversion, the subsidence velocity is constant and set to $W = -Dz_i$, where z_i is the domain-wide-maximum inversion height (here the inversion height is computed as the height of maximum negative vertical gradient of horizontally averaged q_t). As can be seen from the model Eqs. (3)–(7) above, the subsidence velocity is not directly added to the model vertical velocity, but instead is represented as sources in the scalar equations for θ_v and q_t. The subsidence source is omitted from the q_r equation for computational simplicity and its neglect is justified due to the short residence time of rainwater in the simulations. These sources are determined using an upstream advection scheme. The divergent component of the horizontal velocity associated with D is neglected, so that periodic boundary conditions on u can be applied. For domains of size $L = 100$ km or less, the divergent horizontal velocity is $O(DL) \leq 0.5$ m s^{-1}.

e. Relaxation to specified above-inversion sounding

The values of θ_l and q_t between the domain top and six grid points above the mean inversion are relaxed toward specified values. This relaxation allows us to specify the properties of the air being entrained into the inversion from above and control the radiative characteristics of the above-inversion air column without interfering significantly with the dynamics of the boundary layer. In the absence of such relaxation, the above-inversion temperature sounding is prone to slow drift due to imbalances between the clear-air longwave radiative cooling and the subsidence warming. The relaxation is performed by adding the following source terms to the scalar equations:

$$\left.\begin{aligned}\left(\frac{\partial\theta_l}{\partial t}\right)_{\mathrm{relaxation}} &= -\frac{1}{\tau}(\theta_l - \theta_l^0(z))\\ \left(\frac{\partial q_t}{\partial t}\right)_{\mathrm{relaxation}} &= -\frac{1}{\tau}(q_t - q_t^0(z))\end{aligned}\right\}, \quad z > (z_i + 6\Delta z). \quad (10)$$

Here, τ is a relaxation timescale set to 3 h, θ_l^0 and q_t^0 are the specified above-inversion soundings, and Δz is the vertical grid spacing. In the simulations presented here, the specified sounding is time independent and the initial sounding is set equal to this specified sounding. The same procedure can also be used to relax to a time-varying above-inversion sounding, allowing any desired Lagrangian boundary conditions to be specified for the MBL air column.

3. Setup of simulations

a. Boundary conditions

The simulations presented here are designed to model the evolution of a small column of boundary layer air as it advects with the mean wind. In this study, instead of following a trajectory from an actual synoptic case or climatology, we present a somewhat idealized case to isolate the relevant physics in a concise manner. The domain specifications, initial conditions, and boundary conditions are given in Table 1. The boundary and initial conditions are similar to Krueger et al. (1995a) but have been modified to better match Ocean Weather Station (OWS) N climatology (Klein et al. 1995). Our 10-day simulations start with an SST of 285 K, and the SST increases at a rate of 1.5 K day^{-1}, which is typical of summertime climatological trajectories in subtropical stratocumulus regions (Klein et al. 1995). All other boundary conditions are kept fixed. Our upper-air temperature sounding is based on the July-mean Oakland sounding (Schubert et al. 1979) with the above inversion temperature uniformly reduced by 6° to approximate the mean Ocean Weather Station N sounding (Klein et al. 1995). During the course of the simulations, the above-inversion sounding is held constant by the relaxation method described above.

In the course of such a simulation, the lower-tropospheric stability (Klein and Hartmann 1993), defined here as θ (z = 3 km) − SST, varies from about 20 to 5 K. According to July subtropical climatology (Neiburger et al. 1961; Klein and Hartmann 1993), a typical summertime trajectory encounters a significant change in large-scale subsidence, from a divergence $D = 5$ or 6×10^{-6} s^{-1} down to near zero as the column moves

TABLE 1. Base simulation parameters.

Type	Parameter	Value(s)
Numerical	Domain height	3 km
	Domain width	4 km
	Horizontal grid spacing	50 m
	Vertical grid spacing	25 m
	Length of simulation	10 days
	Time step	5 s
Boundary conditions	SST	285 K + (1.5 K day^{-1})
	Reference surface pressure	1021 mb
	Free tropospheric θ_l	296.3 + (3.36 K km^{-1})
	Free tropospheric q_t	3.5 g kg^{-1}
	Divergence (D)	3×10^{-6} s^{-1}
	Geostrophic wind	7.1 m s^{-1} oriented 45° to right of x axis
	Latitude	30°N
	Water vapor path above 3 km	4 kg m^{-2}
	Daily average insolation at 3 km	462 W m^{-2} (solar zenith angle of 69°)
	Downgoing LW radiation at 3 km	214 W m^{-2}
	Radiative/microphysical droplet concentration (N)	50 cm^{-3}
Initial conditions	Boundary layer θ_l	283.7 K
	Boundary layer q_t	7 g kg^{-1}
	Boundary layer depth	600 m
	Wind velocity	geostrophic wind velocity

into the Tropics (some MBL columns experience large-scale convergence). This strong variation has the effect of significantly increasing the MBL depth, as pointed out by Schubert et al. (1979) and others. Since MBL depth is a primary factor in decoupling (BW97) and affects the nature of cumulus convection, the changing divergence could play a significant role in the STCT. However, the divergence is held constant in our simulations, with $D = 3.0 \times 10^{-6}$ s^{-1} in order to better illustrate the effect of rising SST on the STCT, and to simplify the interpretation of the results. An alternative subsidence scheme, using a vertically uniform subsidence velocity, will be explored in a forthcoming sensitivity study.

The simulation is initialized with a cloud-topped mixed layer 600 m deep, with an initial inversion strength of 14 K. This MBL is initially in a nearly steady state. In a test simulation with constant SST, the MBL reaches a steady-state depth of about 700 m with a 150-m thick solid stratocumulus layer in less than 24 h.

Both observations (Minnis et al. 1992; Bretherton et al. 1995) and prior modeling studies (Turton and Nicholls 1987; Bougeault 1985) suggest that the diurnal cycle of insolation is an important factor in determining fractional cloudiness. To separate the effects of rising SST from the effects of the diurnal cycle, we perform two base simulations: ''Cbase'' with constant solar zenith angle chosen to provide the diurnally averaged insolation on 1 July at 30°N and ''Dbase'' using the full diurnal cycle of radiation. After examining Cbase and Dbase, we present a conceptual model and compare this model with Cbase.

The circulations induced by cumulus convection often horizontally span the model domain, so the horizontal width of the domain may be having an effect on the morphology of the clouds. To demonstrate the effect that this has on boundary layer dynamics and fractional cloudiness, we performed an additional simulation, ''Cwide,'' with a domain 12 km wide instead of 4 km wide, which is discussed in section 7.

b. Diagnostic statistics

Two statistics are used to diagnose cloudiness in our simulations: the ''absolute fractional cloudiness'' (AFC) and the ''satellite fractional cloudiness'' (SFC). AFC is the fraction of vertical columns in the model domain that have cloud liquid water. The SFC, which mimics the fractional cloudiness estimates made by use of satellite imagery, is the fraction of vertical columns in the model domain that have an optical depth greater than some visible reflectance threshold [computed as in Austin et al. (1995)]. The optical depth τ for each vertical column is computed using the formula

$$\tau = \frac{3\text{LWP}}{2\rho_l r_{\text{eff}}}, \tag{11}$$

where LWP is the liquid water path and r_{eff} is the radiative effective mean radius (defined in the appendix). The optical depth threshold for SFC is set to 2.5, which corresponds to a shortwave reflectance threshold of 0.12.

To assess the degree of decoupling and MBL thermal stratification, we make simple estimates of the vertical stratification of q_t and θ_l in the MBL. Starting with the horizontal mean soundings (denoted here by $\langle q_t \rangle$ and $\langle \theta_l \rangle$), we take the vertical averages of each in a 75-m thick layer at the surface and in a 75-m thick layer just below the inversion. We define $\Delta q_{t\text{BL}}$ and $\Delta \theta_{l\text{BL}}$ as the

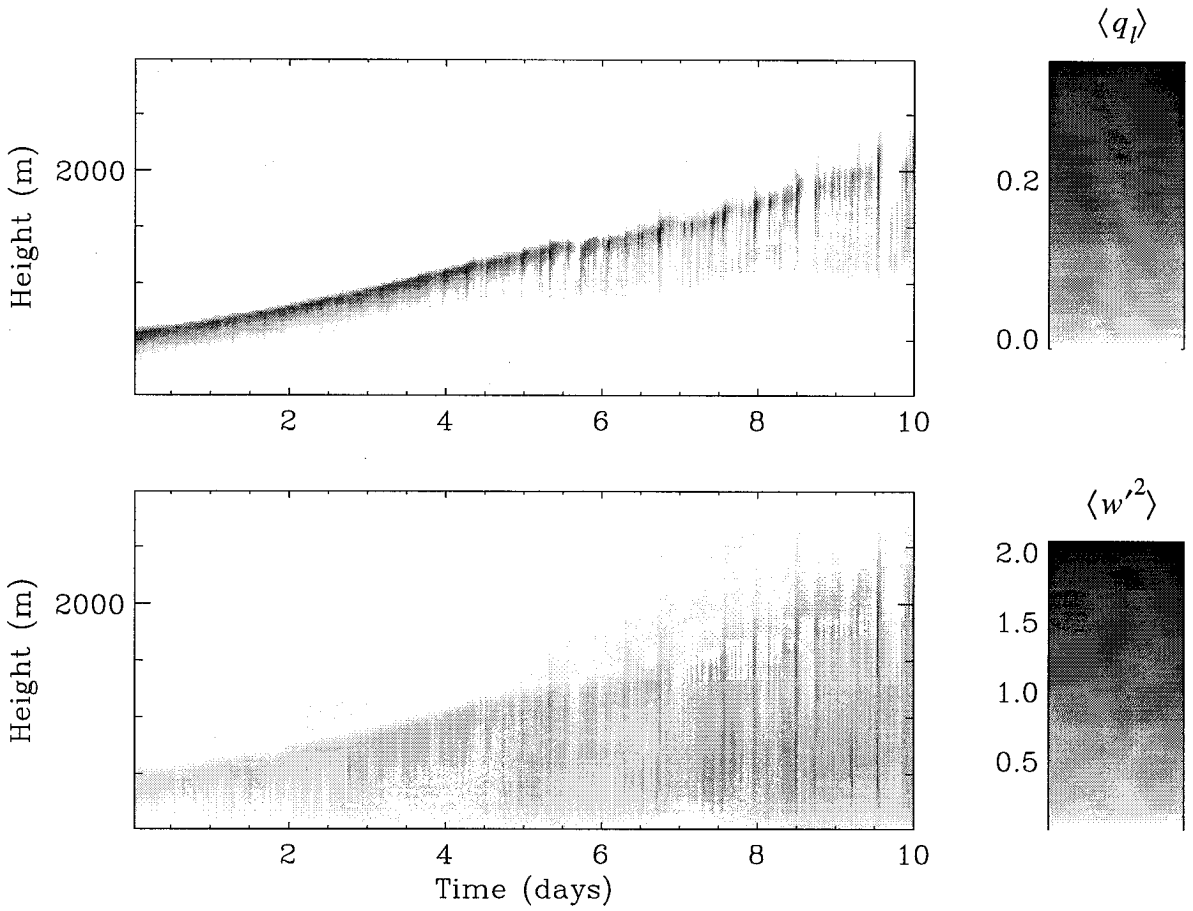

FIG. 1. Time evolution of profiles for the simulation Cbase: (a) $\langle q_l \rangle$ (g kg^{-1}) and (b) $\langle w'^2 \rangle$ (m^2 s^{-2}).

differences in $\langle q_t \rangle$ and $\langle \theta_l \rangle$, respectively, between the surface and the boundary-layer top:

$$\Delta q_{t\mathrm{BL}} \equiv \langle q_t \rangle_{\mathrm{surface}} - \langle q_t \rangle_{\mathrm{BLtop}}$$
$$\Delta \theta_{l\mathrm{BL}} \equiv \langle \theta_l \rangle_{\mathrm{BLtop}} - \langle \theta_l \rangle_{\mathrm{surface}}. \quad (12)$$

Increasing $\Delta q_{t\mathrm{BL}}$ or $\Delta \theta_{l\mathrm{BL}}$ indicates more decoupling and internal boundary layer stratification.

The MBL-top entrainment rate is calculated from the time variation of the inversion height, z_i. For our simulations, a very accurate measure of z_i can be found from the total water field. At all times, the contour $q_T = 5$ g kg^{-1} is within the inversion. For each grid column, we determine the local inversion height $z_{i,\mathrm{column}}$ at which $q_T = 5$ g kg^{-1} using linear interpolation between the bracketing grid points. Here, z_i is the average of $z_{i,\mathrm{column}}$ over all columns.

The buoyancy flux $g\langle w'\theta_v' \rangle/\bar{\theta}$ is the dominant source of turbulent kinetic energy (TKE) in buoyantly driven boundary layers. It is scaled to units of W m^{-2} by multiplying by $\bar{\rho} C_p \bar{\theta}/g$. The buoyancy flux is computed here from the product of the perturbation fields of w and θ_v; it is not a "true" model flux. Other model fluxes presented are "true" fluxes fully consistent with the discrete transport schemes.

4. Base simulation results

a. Constant solar zenith angle: Cbase

Figures 1 and 2 show the evolution of the boundary layer in Cbase. Figure 1 shows time–height sections of $\langle q_l \rangle$ and the vertical velocity variance $\langle w'^2 \rangle$. Figure 2 shows the soundings of $\langle \theta_l \rangle$, $\langle \theta_v \rangle$, $\langle q_t \rangle$, and $\langle q_l \rangle$. The boundary layer deepens from 600 m to 2300 m over the 10-day simulation due to the increase of the SST relative to the constant above-inversion temperatures. The θ_l inversion strength is reduced from about 14 K to 4 K over the duration of the simulation, and there is a gradual increase of the mean entrainment rate through the MBL top from 3 to 9 mm s^{-1}.

The simulated transition can be divided into three stages, a shallow well-mixed stratocumulus topped boundary layer (days 0–3), a deeper decoupled boundary layer with cumulus rising into stratocumulus clouds (days 3–8), and an even deeper trade-cumulus boundary

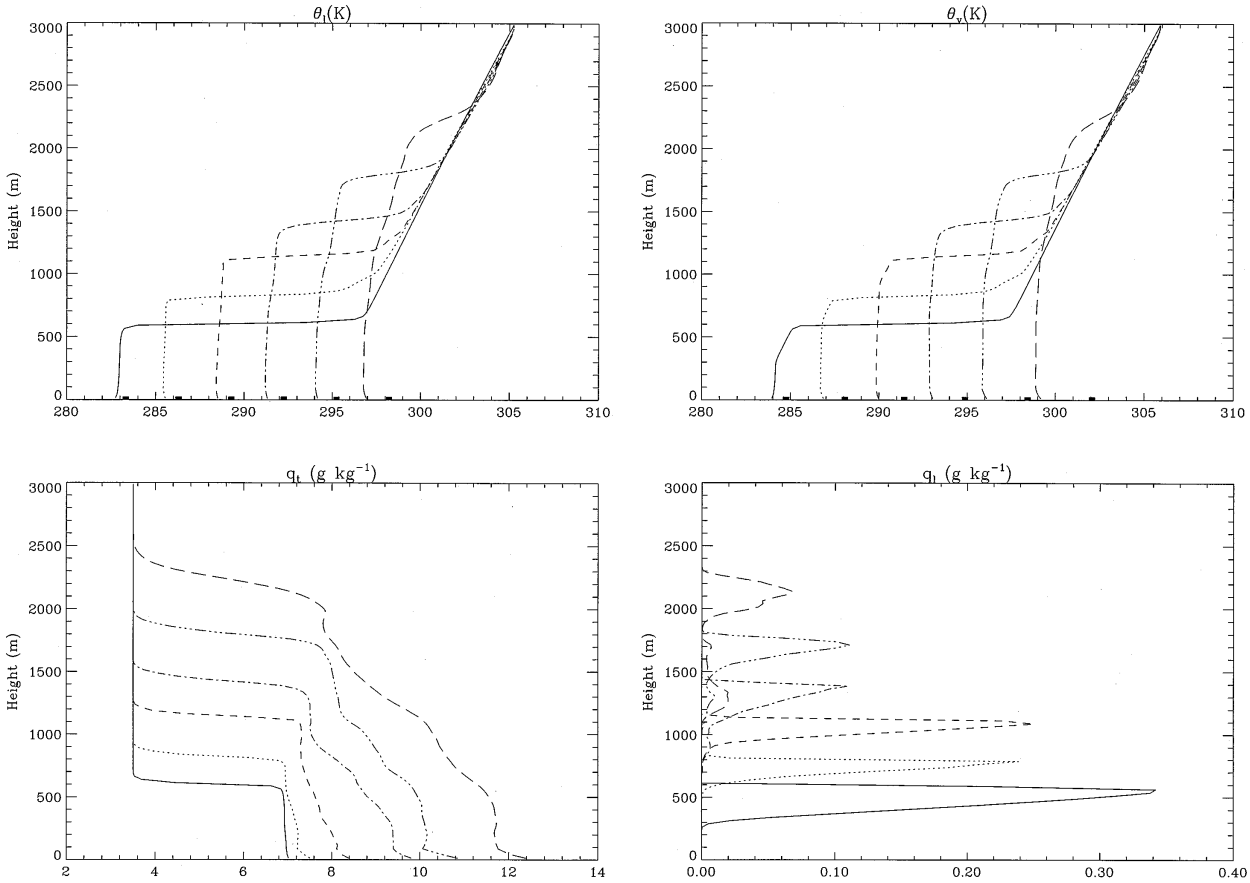

FIG. 2. Horizontal mean soundings from Cbase at day 0 (solid), day 2 (short dashed), day 4 (long dashed), day 6 (long-short dashed), day 8 (long dashed–three-short dashed), and day 10 (very long dashed). (a) $\langle\theta_l\rangle$ with rectangles plotted at θ (p_0, SST) for each sounding time; (b) $\langle\theta_v\rangle$ with rectangles plotted at θ_v (p_0, SST, q_{sat}) for each sounding time; (c) $\langle q_t\rangle$; (d) $\langle q_l\rangle$.

layer without much overlying stratocumulus (days 8–10). These stages were also discussed by Krueger et al. (1995a,b).

In the well-mixed stratocumulus-capped MBL, the cloud is nearly horizontally homogeneous stratocumulus about 200 m thick. The horizontal variations in cloud-base height are only about 50 m and variations in cloud-top height are even smaller. The profile of q_l is very nearly adiabatic, with a maximum q_l at cloud top of 0.25 g kg^{-1} after the first few hours.

Decoupling is initially manifested as an increased raggedness of cloudbase in days 3–4 as updraft and downdraft LCLs become more disparate. Associated with decoupling is a splitting of the vertical profile of $\langle w'^2\rangle$ into two separate maxima after day 3, one below the lowest clouds and one near the inversion (Fig. 1b). As the MBL deepens, $\langle w'^2\rangle$ becomes intermittent, with more intense peaks. This reflects sporadic cumulus convection with increasingly strong updrafts as the conditionally unstable layer deepens. The soundings in Fig. 2c show that the vertical gradient of q_t is small for day 2, indicative of a mixed layer, and then increases throughout the remainder of the simulation. The θ_l sounding from day 2 is also well mixed. In the θ_l and θ_v soundings from day 4 onward, a thin ''transition layer'' of stable stratification is seen above cloud base, as in trade cumulus cloud fields. Above the transition layer, the stratification is also stable but remains very weak until the stratocumulus layer becomes broken (day 8 and day 10 soundings).

These trends are quantified in higher time resolution in Fig. 3, which shows the decoupling indicator $\Delta q_{t\mathrm{BL}}$ and the total boundary layer stratification $\Delta\theta_{l\mathrm{BL}}$ (both defined in section 3b; Cbase results are the solid lines). The change from the well-mixed stratocumulus MBL to cumulus rising into stratocumulus (CuSc) is gradual. Both $\Delta q_{t\mathrm{BL}}$ and $\Delta\theta_{l\mathrm{BL}}$ remain small and relatively constant for the first 2.5 days, indicating a well-mixed boundary layer, but increase gradually from days 2.5 to 5 and more rapidly in days 8–10 after the stratocumulus cloud layer becomes broken.

A typical flow field early in the CuSc phase at day 4.5 is shown in Fig. 4, plotted in the model translating frame. The boundary of the cloud is outlined (defined as the contour where $q_l = 0.01$ g kg^{-1}), and the q_t field is shaded. In the center of the domain a cumulus cloud

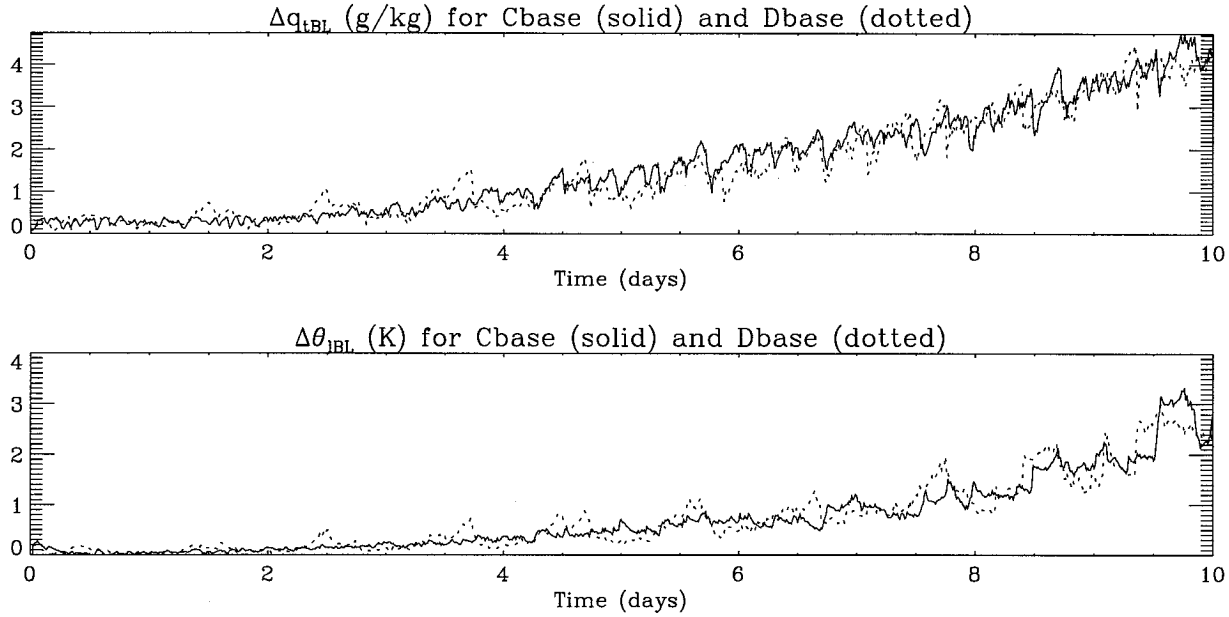

FIG. 3. Time series of decoupling indicators for Cbase (solid) and Dbase (dotted): (a) $\Delta q_{t\mathrm{BL}}$; (b) $\Delta\theta_{j\mathrm{BL}}$.

has reached the inversion at 1200 m and is detraining moist air to the right, helping to maintain a stratocumulus layer. The q_t field shows large horizontal and vertical variability; the interface between the moist surface layer and the upper MBL is irregular in shape and height. Also apparent in the figure is the substantial mean shear of u momentum that develops throughout Cbase. We suspect that this shear is an artifact of the two-dimensionality of the simulation. The implications of this shear are discussed briefly in section 7.

In Cbase, turbulent kinetic energy is generated primarily by positive buoyancy fluxes. Nicholls (1984) suggested that decoupling occurs when the maintenance of a mixed layer requires buoyancy fluxes to be negative over a substantial height range. Figure 5a shows the 2-h averaged buoyancy fluxes at 24-h intervals through day 4. The positive buoyancy fluxes within the stratocumulus cloud layer increase slightly though erratically with time. However, a layer of negative buoyancy fluxes below cloudbase develops and thickens after day 2. (The small positive spike in buoyancy flux at the inversion top is an artifact of numerical discretization.)

BW97 point out that the increasing difference between in-cloud and subcloud buoyancy fluxes seen in Fig. 5a is due to the increasing latent heat fluxes within the MBL and attribute decoupling primarily to the increasing latent heat fluxes caused by the SST increase. In days 1 and 2 when the boundary layer is still well coupled, the jump in buoyancy fluxes at cloudbase increases proportional to the rate of increase of latent heat fluxes in the MBL (shown later) as predicted by Eq. (9) in BW97. The buoyancy flux jump at cloudbase continues to increase after decoupling in days 3 and 4 (even though the BW97 condition no longer strictly applies) but deviates substantially from BW97's formula after day 4 as the cumuli become deeper and better defined.

The buoyancy fluxes after day 4 (Fig. 5b) are more irregular and tied to cumulus convection. In addition to the positive buoyancy fluxes near the inversion due to stratocumulus, cumulus convection during these later times creates both positive buoyancy fluxes over large depths, and negative buoyancy fluxes in the middle depths of the MBL through compensating subsidence.

In Fig. 6, lightly smoothed time series of the minimum subcloud and maximum in-cloud buoyancy flux are plotted together with the buoyancy integral ratio BIR (BW97). The BIR in the model is defined as the negative of the ratio of the vertical integral of the buoyancy flux over the range of heights where it is both negative and below cloud (below the level of maximum areal fraction of cloudy grid points), divided by the vertical integral of the buoyancy flux at all other heights. BW97 suggests a threshold BIR > 0.15 for decoupling.

These time series show that the trends seen in Fig. 5a are quite representative of intermediate times. The buoyancy flux maximum, generally located near the top of the cloud layer, increases slightly during days 0–3. The buoyancy flux minimum, generally located just below cloud base, remains above zero until about day 2, after which time it decreases to about -4 W m^{-2} at day 3 when decoupling occurs. The BIR rises from near zero for days 0–2 up to 0.1–0.15 by day 3, when decoupling first occurs. Our results from Cbase support the link between negative buoyancy fluxes as measured by BIR and decoupling.

After 4 days, the lifting condensation level (LCL) of the updrafts is over 300 m lower than the level of solid stratocumulus. The updrafts become more and more cu-

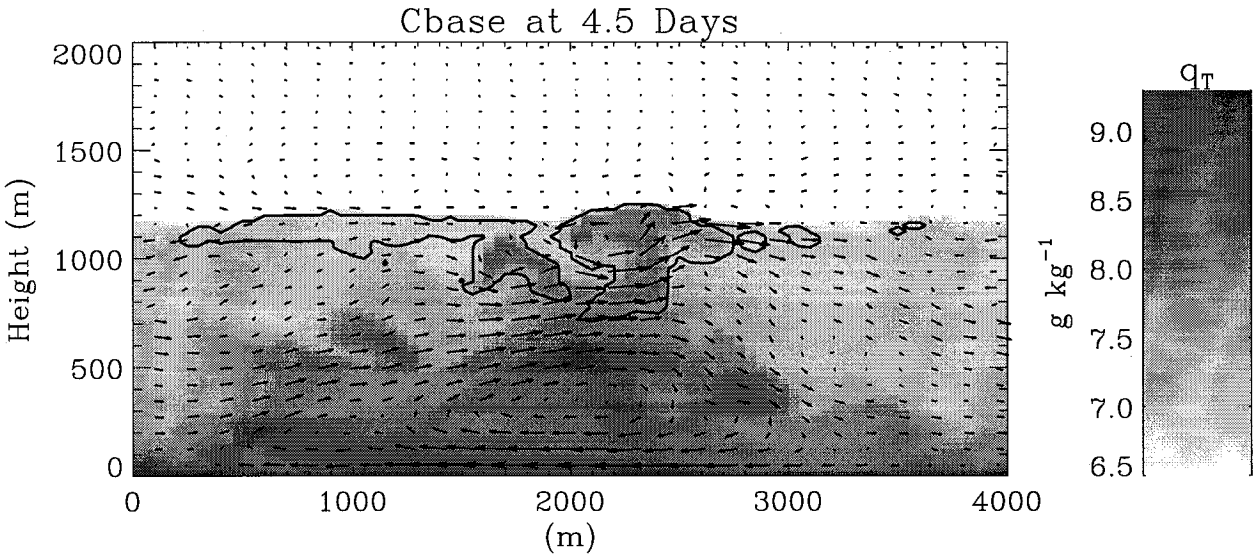

FIG. 4. Vector flow field of u and w at 4.5 days in Cbase in the model reference frame (maximum vector length = 4.0 m s^{-1}). Cloud border is contoured at q_l = 0.01 g kg^{-1}, and the q_t field is shaded. The sea surface velocity is 5.0 m s^{-1} to the left and 5.0 m s^{-1} into the plane of the figure.

muliform, with vertical velocities regularly exceeding 2 m s^{-1}. The LCL of near-surface air, which approximately coincides with the cumulus cloud base, rises only slightly with time, so the depth of cumulus convection rapidly increases as the MBL deepens. The overall cloud structure is no longer horizontally homogeneous, with small areas covered by cumulus updrafts and large areas covered by stratocumulus clouds, which in time become thinner and more patchy. As the boundary layer deepens a secondary peak of $\langle w'^2 \rangle$ appears in the subcloud mixed layer below the cumulus cloud base at around 500 m. Often the cumulus bursts cause a strong enhancement of $\langle w'^2 \rangle$ near the inversion as well.

Figure 7 shows the evolution of fractional cloudiness, the mean liquid water path (LWP), cloud base precipitation, radiative cooling, and surface heat fluxes in Cbase. The fractional cloudiness is measured using SFC and AFC (defined in section 3a). The stratocumulus cloud remains solid throughout the first five days of the simulation with a significant reduction of the cloud cover thereafter. The SFC is much lower than the AFC for days 4–7, showing that much of the stratocumulus is very thin. While the boundary layer is well mixed the LWP (Fig. 7b) remains relatively constant with time. As the boundary layer decouples the mean LWP shows spikes every 3 or 4 h whose amplitude tends to increase with time. The spikes occur within 15 min after maxima of vertical velocity variance $\langle w'^2 \rangle$; they are produced by sporadic cumulus convection which injects liquid water into the upper part of the MBL.

The large variances after day 4 in cloud fraction, liquid water path, precipitation, and buoyancy fluxes are

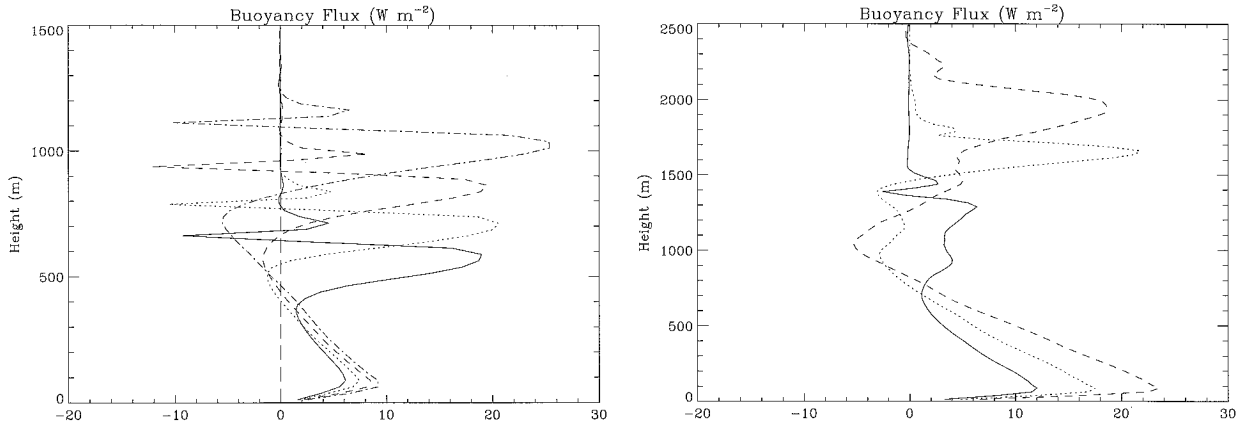

FIG. 5. Buoyancy flux profiles (2-h mean) in Cbase: (a) day 1 (solid), day 2 (dotted), day 3 (dashed), and day 4 (dashed–dotted) [A line is plotted along zero buoyancy flux (dashed) for reference]; (b) day 6 (solid), day 8 (dotted), and day 10 (dashed).

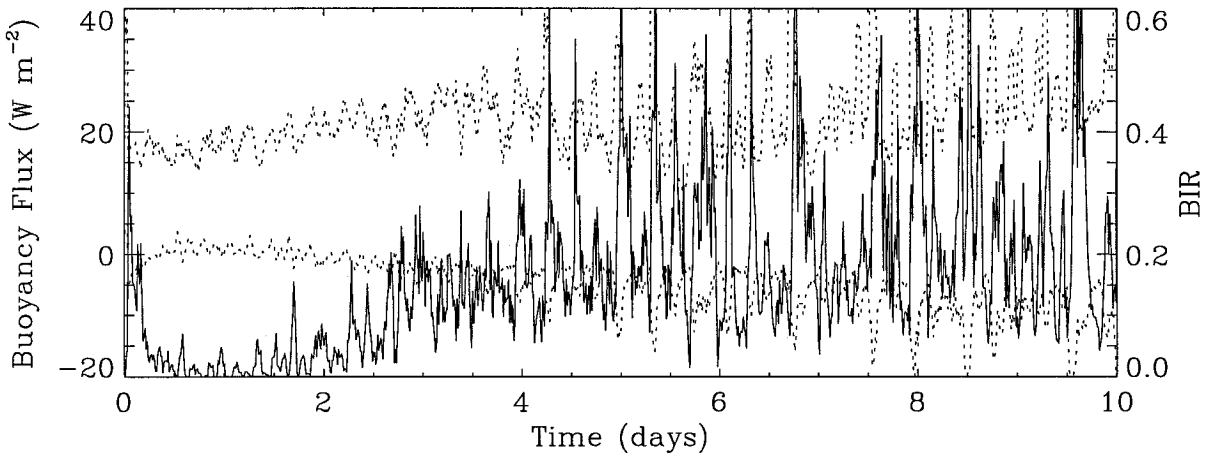

FIG. 6. Cbase 1-h smoothed time series of buoyancy flux maxima and minima (dotted) and buoyancy integral ratio, BIR (solid).

caused by intermittent cumulus convection. This could be related to the simulation domain width being smaller than the natural horizontal spacing of MBL cumulus convection. The effects of widening the model domain are discussed in section 7 in the analysis of Cwide.

The mean precipitation fluxes at cloud-base are plotted in Fig. 7c. The cloud-base precipitation fluxes from the base of the stratiform layer are typically very small, around 0.2 mm day^{-1}. Very little of this precipitation reaches the surface. From day 3 onward, the precipitation increases drastically during cumulus convective bursts, while the precipitation from the stratocumulus becomes weaker with time as the stratocumulus clouds thin. Because of the low stratiform precipitation rates during most of the simulation, the effects of the drizzle-induced condensational heating and evaporative cooling on the overall heat and water budget of the MBL are negligible in Cbase except during cumulus convection. The time-averaged net latent heating due to surface precipitation fluxes remains less than 5 W m^{-2} throughout the simulation. The sensitivity of these results to the assumed concentration of activated cloud condensation nuclei are explored in a forthcoming study.

Heating in the cloud through absorption of shortwave radiation is quickly neutralized by rapid mixing with sinking air that has been strongly cooled by longwave radiation at cloud top. As a result, the critical parameter for MBL structure is the net radiative cooling in the cloud, and increases in shortwave radiative heating are nearly equivalent to reductions in LW cooling (due, e.g., to the presence of upper-level clouds or a moist-free troposphere). However, when the amplitude of the shortwave radiative heating is large compared to longwave cooling, decoupling through shortwave radiative absorption is possible. This is the source of the diurnal decoupling in the double-mixed-layer model of Turton and Nicholls (1987).

The longwave cooling of the MBL (Fig. 7d, dashed) remains relatively constant through day 4 of the simulation with a mean value of 52 ± 5 W m^{-2}. Only where the stratocumulus thickness drops to less than 50 m is there significant diminution of the longwave cooling. The shortwave heating of the MBL is approximately constant at around 15 W m^{-2} through day 4 and increases somewhat when cumulus clouds are present. Thus, the net MBL cooling (Fig. 7d, solid) is steady at about 37 ± 5 W m^{-2} for four days and then fluctuates significantly due to cumulus convection and stratocumulus cloud dissipation. The net cooling below the LCL (Fig. 7d, dotted line) is minuscule before stratocumulus thinning and breakup, after which time it is 0–10 W m^{-2}. During decoupling, neither the shortwave absorption nor the net MBL radiative cooling changes significantly, suggesting that changes in the radiative forcing for convection do not appear to be the impetus for deepening–warming decoupling.

The sensible heat fluxes (Fig. 7e, dashed) are small throughout the length of the simulation. During the first five days, the air–sea temperature difference is approximately constant at about -0.9 K and the sensible heat flux is only about 6 W m^{-2}. After day 5 the magnitude of the air–sea temperature difference increases slowly, reaching -1.4 K, and the sensible heat flux grows to 12 W m^{-2}. The mean surface latent heat fluxes (Fig. 7e, solid) are much larger and increase almost linearly during Cbase, from around 20 W m^{-2} to 180 W m^{-2}. This increase is due to the rapid increase of saturation vapor pressure of the surface air as the MBL warms with the rising SST and is also due to the increasing entrainment of dry air from above the inversion as Cbase proceeds. These effects also cause the minimum cloud base to increase from 350 m to 1100 m over the course of the simulation as the near-surface lifted condensation level rises. The latent heat fluxes throughout the depth of the MBL (not shown) are nearly constant with height at most stages of Cbase, and increase in conjunction with the surface latent heat fluxes. Their large increase pro-

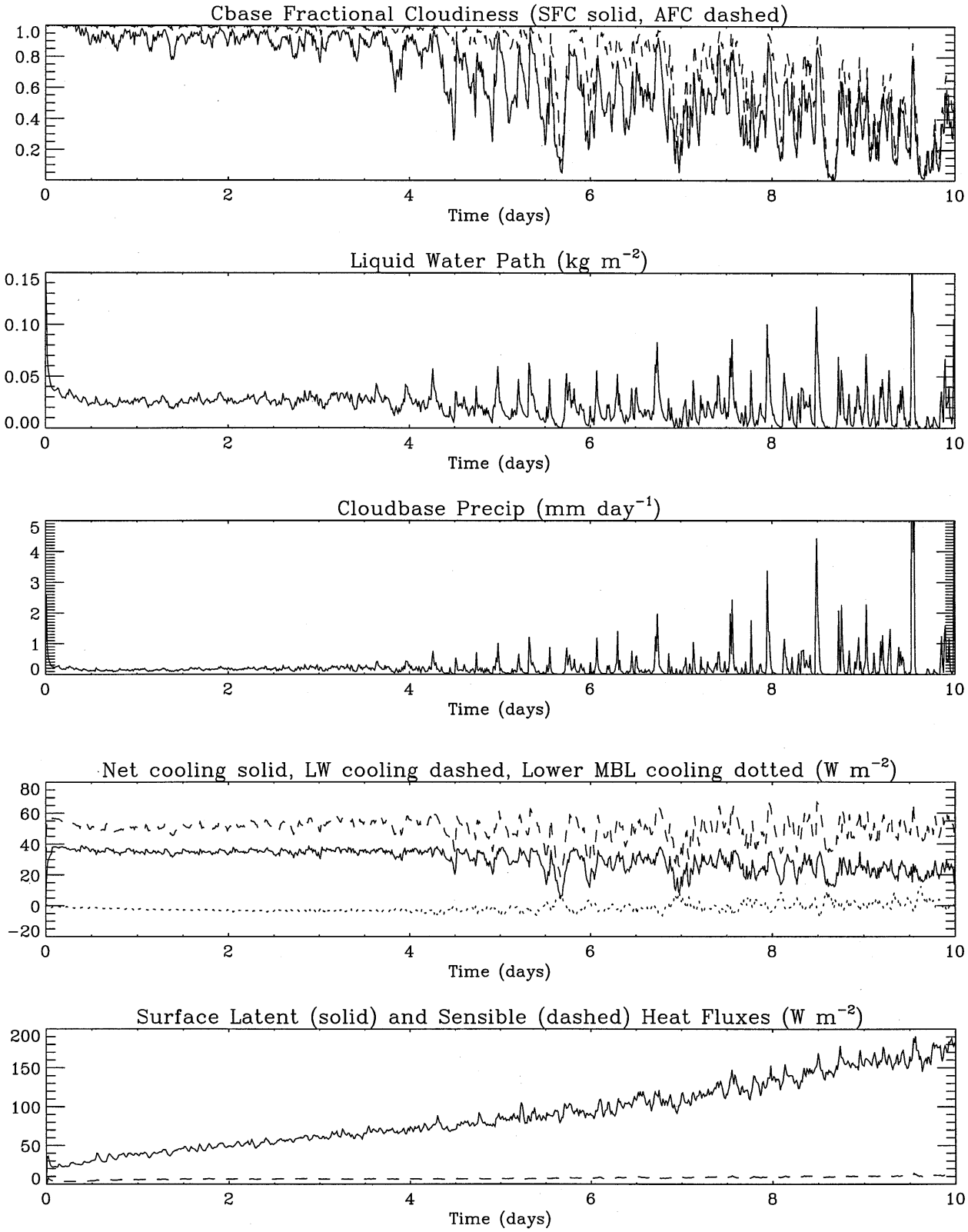

FIG. 7. Time series of Cbase: (a) fractional cloudiness statistics, SFC (solid), AFC (dashed); (b) horizontal mean liquid water path; (c) cloud-base precipitation; (d) net MBL radiative cooling (solid), MBL longwave cooling (dashed), lower MBL radiative cooling (dotted); (e) surface latent (solid) and sensible (dashed) heat fluxes.

TABLE 2. Comparison of simulations (Cbase and KSCT) and climatologies [satellite (SAT), Warren et al. (1992), and Ocean Weather Station N] for several values of lower-tropospheric stability (S). The cloud fraction from Warren et al. (1992) is separated into $\sigma_{Sc} + \sigma_{Cu}$.

	Cloud fraction (%)					Cloud-top height (m)			
S (K)	Cbase (SFC)	KSCT	SAT	Warren	OWS N	Cbase	KSCT	SAT	OWS N
21	90	>90	67	64 + 7		650	900	1050	
18	90	>90	68	47 + 10		880	1250	1350	
15	65	50	53	30 + 15	68	1250	1550	1650	1450
13	50	25	27	18 + 19		1450	1800	2000	

motes the increase in BIR and decoupling, as discussed above.

The subgrid-scale fluxes of heat and moisture are very small throughout Cbase and reach a maximum of 5% of the resolved fluxes at all heights in the MBL.

b. Comparison of Cbase with other simulations and observations

The simulation Cbase can be compared to the simulations "SCT_1" and "SCT_2" of Krueger et al. (1995a) (the combination of the two will hereafter be referred to as KSCT). The KSCT simulations have the same subsidence and surface wind forcing and nearly identical radiative forcing, but do not include any form of precipitation. In KSCT the SST increases from 290.2 K at a rate of 1.8 K day^{-1} for six days, 20% faster than in Cbase. The most significant difference is that the initial temperature above the inversion is about 5 K warmer in KSCT than in Cbase, with the same lapse rate. In KSCT, the free-tropospheric sounding is maintained only at the domain top (3 km in SCT_2) and allowed to drift to a radiative–subsidence balance below this level. A deep dry-adiabatic layer rapidly forms above the inversion, resulting in a much higher free-tropospheric lapse rate than in Cbase. Initially the boundary layer depth is about 800 m in KSCT, midway between the 600-m initial depth in Cbase and the 1100-m MBL depth in Cbase after 3½ days, when the SST = 290.2. Despite these differences in initialization, boundary conditions, and model formulation, both simulations show a similar transition to decoupling as the boundary layer deepens, followed by development of CuSc, and eventual dissipation of the overlying stratocumulus.

However, the timing of these stages is not the same in the two simulations. Other simulations we have performed show that the cloudiness transition is better correlated to the lower-tropospheric stability

$$S = \theta(700 \text{ mb}) - \text{SST}, \tag{13}$$

than to SST alone, in agreement with Klein and Hartmann's (1993) climatology. Our definition of S differs marginally from that of Klein and Hartmann in using SST in place of surface temperature since the former is more widely documented. Since mean air–sea differences are observed to be well under 1 K in the eastern subtropical oceans (Betts et al. 1992), this difference is negligible. For Cbase, θ(700 mb) = 307 K, while for KSCT, θ(700 mb) = 312 K.

Table 2 compares cloud cover and mean cloud-top height (assumed to be the same as the height of the inversion base) in KSCT and Cbase with three observational climatologies for several different values of S. The first (SAT) climatology is based on Betts et al.'s (1992) satellite retrievals of low cloud fraction and cloud-top height over the subtropical northeast Pacific Ocean (including most of the region 10°–35°N, 115°–145°W), binned by SST. For all of their SST bins, θ(700 mb) = 314 ± 0.5 K. The second ("Warren") climatology includes the low lying stratus + stratocumulus + fog and cumulus cloud amounts from routine surface cloud observations compiled in the Warren et al. (1988) cloud atlas. The stratus cloud amount is taken from the regression of Klein and Hartmann (1993), while the cumulus cloud amount was derived by superimposing the June–July–August (JJA) climatology of S of Klein and Hartmann on the JJA cumulus cloud amount from the Warren cloud atlas. We computed the mean cumulus cloud amount around a given contour of S, averaged over the four subtropical stratocumulus regions—the west coasts of North and South America, near the Canary Islands, and off Namibia. In Table 2, the cloud fractions are tabulated in the form $\sigma_{Sc} + \sigma_{Cu}$, where σ_{Sc} and σ_{Cu} are the stratus and cumulus cloud fractions. The last ("Ship N") climatology (Klein et al. 1995) is the daily average cloudiness and the inversion base from the composite JJA "cold advection" sounding from 27 years of routine cloud observations and soundings at Ocean Weather Station N (30°N, 140°W). This sounding has θ(700 mb) = 310 K and SST = 295 K.

The free-tropospheric sounding used for Cbase was chosen to match the OWS N temperature just above the inversion top at 800 mb, while maintaining KSCT's initial lapse rate. Since the OWS N 700–800 mb mean lapse rate is lower than in KSCT, θ(700 mb) is larger in the Ship N sounding than in Cbase. This illustrates a difficulty in using S to characterize the free-tropospheric structure, namely that the actual above-inversion temperature (which is the upper boundary condition on the boundary layer dynamics) depends on the lapse rate below 700 mb as well as the 700-mb temperature itself. In addition, the mean wind speed and horizontal divergence in these climatologies are not the same as in Cbase or KSCT, and the climatologies incorporate a variety of

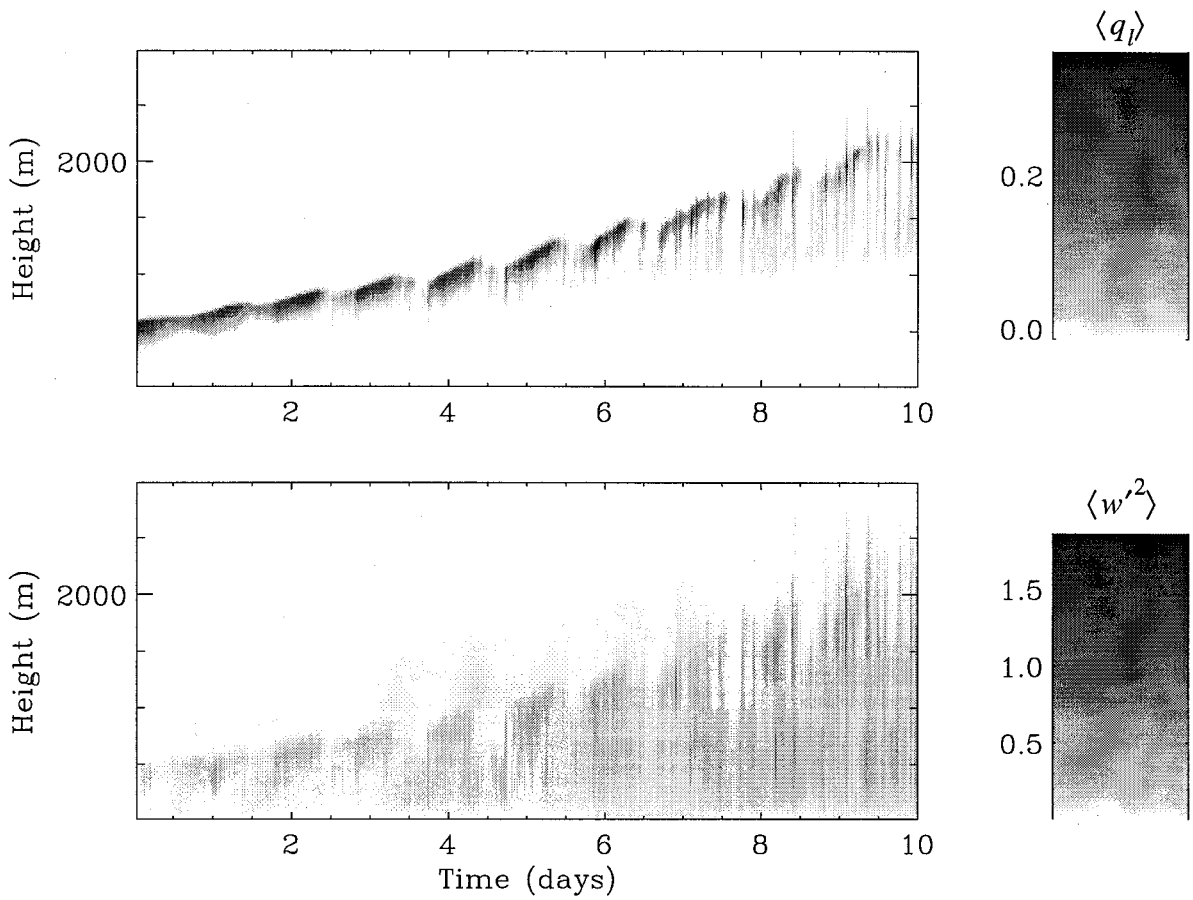

FIG. 8. Time evolution of profiles for the simulation Dbase: (a) $\langle q_l \rangle$ (g kg^{-1}); (b) $\langle w'^2 \rangle$ (m^2 s^{-2}).

synoptic situations, so exact agreement between the observations and the models cannot be expected even if the models were perfect.

In Table 2, the cloud fraction listed for Cbase is the SFC smoothed over a 12-h interval centered at the time at which the specified S was attained. For KSCT, the tabulated cloud fraction is the maximum overall heights of the fraction of grid points at that height which contain cloud. In KSCT, this cloud fraction dips below 0.5 after 4 days, when the SST = 297 K and S = 15 K. In Cbase, the time-smoothed SFC decreases to 0.5 after 6 days (SST = 294 K, S = 13 K), while the smoothed AFC (not tabulated) decreases to 0.5 only after 8.5 days (SST = 298 K, S = 9 K). Thus the cloudiness transition occurs at a somewhat lower S in Cbase than in KSCT. Correspondingly, the boundary layer depth in Cbase at a given S is lower than in KSCT.

Both models predict much higher cloud fractions than the climatologies at high S. This can be partly ascribed to the cold advection (rising SST) used in the simulations, which is particularly favorable for boundary layer cloudiness (e.g., Klein et al. 1995). Meanwhile, the climatologies involve measurements encompassing both warm and cold advection. In the satellite and Warren climatologies, a cloud fraction of 50% corresponds to an S of approximately 15 K, in better greement with KSCT than Cbase. The satellite cloud-top heights are slightly greater than in KSCT and substantially greater than in Cbase. However, the OWS N cold advection climatology at the same S, which focuses more exclusively on the situation being modeled by Cbase and KSCT, has a much higher cloud fraction, comparable to Cbase, and a lower inversion base, which lies between the predictions of KSCT and Cbase. In summary, the results from the two models are qualitatively similar but quantitatively slightly different, and both models are plausible descriptions of the observed stratocumulus to trade cumulus transition.

c. Diurnal radiation: Dbase

We now turn to the case with diurnal radiation, Dbase. The overall evolution of the boundary layer in Dbase, shown in Figs. 8 and 9, is quite similar to Cbase, with diurnal variations modulating the same systematic evolution. The diurnal cycle does not appear to be fundamentally important for the systematic changes in cloud amount and type that take place in the STCT. The 1700

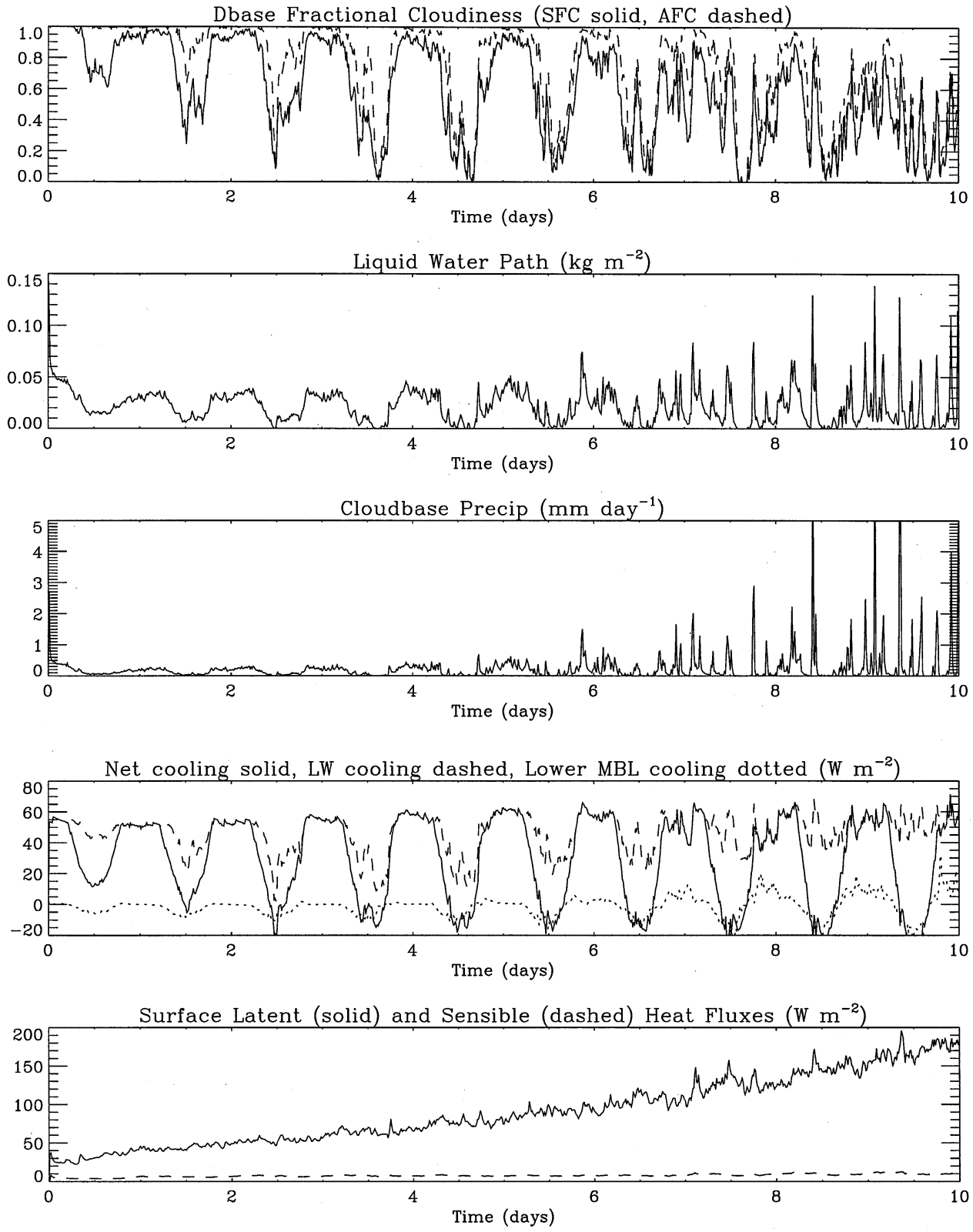

FIG. 9. As in Fig. 7 except for the Dbase simulation.

m deepening of the boundary layer during Dbase is nearly identical to that observed in Cbase, as are the mean evolution of the soundings of $\langle \theta_l \rangle$ and $\langle q_t \rangle$. The diurnally averaged cloud thickness in Dbase is quite similar to the cloud thickness in Cbase, as are long-term changes in cloud type and boundary layer structure. The decoupling and stability parameters for Dbase (Fig. 3, dotted line) increase almost in lock step with those of Cbase over the 10-day length of the simulation as do the surface heat and moisture fluxes (Fig. 9e).

Afternoon cloud thinning occurs due to decoupling driven by shortwave heating in the cloud. Starting on the second day there is significant afternoon clearing, which increases in magnitude and duration as the simulation proceeds (Figs. 8a and 9a). The radiative effect of the daytime shortwave heating is amplified by the reduction in longwave cooling as the stratocumulus thins or evaporates (Fig. 9d, dashed line). The cumulative effect is a drastic reduction in the net MBL cooling during the daytime (Fig. 9d, solid line) becoming more pronounced each day. These effects reduce the buoyant production of TKE, especially below the stratocumulus cloud layer, resulting in a pronounced afternoon minimum in $\langle w'^2 \rangle$ (Fig. 8b). After the sun sets, longwave cooling at the cloud top (or the upper MBL if clouds are completely absent) revitalizes convection. This leads to reformation or thickening of stratocumulus cloud, often reinforced by an unusually vigorous cumulus burst.

The diurnal cycle is strongly evident in the MBL-entrainment rate (not shown). During the first two days the entrainment rate fluctuates from about 2 mm s^{-1} during the day to 4 mm s^{-1} at night. As the simulation progresses, the entrainment rate drops to nearly zero during the afternoon clearings and grows progressively larger each night.

Starting at day 7 of the simulation, there is significant clearing at nighttime as well, though the diurnal radiative forcing still heavily modulates the fractional cloudiness. In these late stages of Dbase, the occurrence of cumulus cloud bursts is fairly evenly distributed over the diurnal cycle. The changes in cloudiness relate instead to the lifetimes of the stratocumulus clouds detrained near the MBL-top by the cumulus clouds; during the daytime the solar absorption by the stratocumulus clouds keeps their lifetimes much shorter than at night.

5. A conceptual model of the STCT

We now present a conceptual model of the STCT, DIDECUPE (Deepening-Induced Decoupling and Cumulus Penetrative Entrainment), sketched in Fig. 10, which explains the main features of both our modeling results and of observations. The starting point of this model (Bretherton 1992) is that the transition in cloudiness occurs in two steps, as seen in Cbase. They are 1) deepening–warming decoupling of a shallow cloud-topped mixed layer into a regime characterized by CuSc,

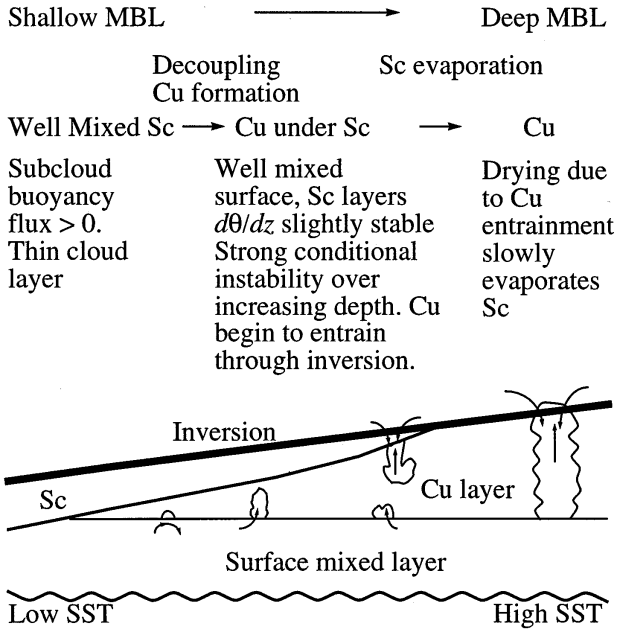

FIG. 10. A conceptual diagram of the STCT.

and 2) increasingly vigorous penetrative entrainment of dry free-tropospheric air by the cumulus, which eventually evaporates the stratocumulus and exposes the underlying trade cumulus cloud layer. Figure 10 is a schematic illustration of the essential feedbacks involved in the two-step conceptual model of the STCT.

These steps follow inexorably from the systematic downstream deepening of the MBL following boundary layer air parcel trajectories, driven by the downstream decrease in lower-tropospheric stability and by decreasing mean subsidence. Other processes such as precipitation, the diurnal cycle, systematic changes in insolation or mean upper-level mixing ratio, and changing surface winds are important in actually determining fractional cloudiness as a function of position, but are not required for the MBL transition. We now consider the dynamics responsible for the two steps in more detail.

A mechanism for the first step, the decoupling transition, is discussed in a companion paper (BW97) and borne out in the brief analysis of Cbase presented above. Summarizing this mechanism, a buoyancy-driven mixed layer can be maintained only if the generation of eddy kinetic energy by buoyancy fluxes is predominantly positive throughout most of the mixed layer. As SST warms and the MBL deepens, upward latent heat fluxes in the boundary layer increase dramatically. This increases the buoyancy fluxes and turbulence levels within the cloud, creating more entrainment per unit of cloud radiative cooling. The increased entrainment leads to increasingly negative buoyancy fluxes below cloudbase associated with a downward flux of warm entrained air. This disrupts the mixed layer and creates a weak stable layer

below cloud base. The stable layer acts as a valve that allows only the most powerful subcloud-layer updrafts to penetrate up to the main stratocumulus cloud base. As the decoupling becomes more pronounced, the updrafts resemble small cumuli.

The second step in the STCT, the evaporation of the upper stratocumulus layer, will be our focus for the remainder of this paper. While the cumulus clouds sustain the stratocumulus by detrainment of liquid water near the inversion, we suggest that they also cause its ultimate demise. Within the cumulus layer, the stratification is much weaker than moist adiabatic, so conditional available potential energy (CAPE) builds up rapidly as the cumulus layer deepens. The DIDECUPE hypothesis holds that penetrative entrainment of dry free tropospheric air by increasingly vigorous cumulus clouds evaporates most of the liquid water in the updraft before it is detrained, leaving smaller and smaller stratocumulus cloud patches around the cumulus. The ratio of penetratively entrained mass flux of dry air to upward cumulus mass flux of moist surface-layer air increases, drying the cloud layer. This process is gradual and involves the formation of mesoscale and smaller scale holes in a thinning cloud sheet that eventually reveal the cumulus cloud field below. Satellite photos of the STCT (Klein et al. 1995) are consistent with such a view.

Weak stratification in the cumulus layer is a fundamental feature of the CuSc regime, reflecting the radiative–convective balance that occurs beneath the stratocumulus. It arises as follows: To carry the moisture flux that sustains the overlying stratocumulus, there must be a significant cumulus mass flux and hence significant compensating subsidence in the environment. In a trade-cumulus regime, the clear air between cumulus clouds radiatively cools 2–3 K day^{-1} as it slowly subsides creating stable stratification. However, in the CuSc regime the overlying stratocumulus blanket prevents significant radiative cooling below the stratocumulus base. Since the compensating subsidence around cumulus clouds is still strong, the thermal stratification within the cumulus layer is weak. Therefore, in the CuSc regime, the conditional instability increases rapidly as the cumulus layer deepens.

Even in the absence of vertically distributed radiative cooling, slight stratification in a cumulus layer can occur if the SST is rising following the boundary layer air and the cumuli detrain mainly at the top of the cumulus layer into and just below the inversion. Because the entire boundary layer warms nearly in step with the SST, the temperature profile below the cumulus detrainment layer can be changed only by vertical advection, assuming there is no radiative cooling there. Given typical cumulus mass fluxes of 2 cm s^{-1} inferred from observations of a transitional cloud regime in ASTEX (Bretherton et al. 1995) and a warming rate of 1–2 K day^{-1}, the required stratification is 0.5–1 K km^{-1}. This stratification is still much weaker than moist adiabatic and therefore has little impact on the growth of CAPE with cumulus layer depth.

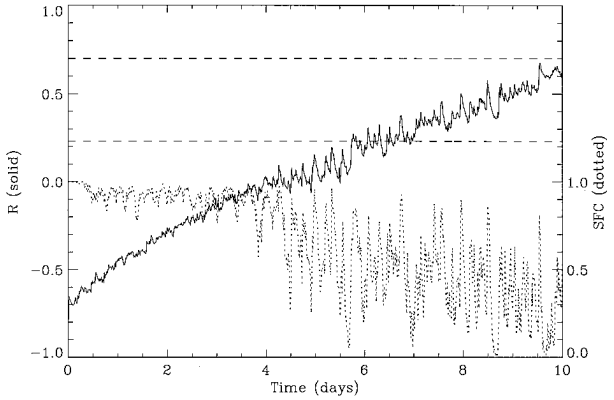

FIG. 11. Time series for Cbase of the CTEI criteria R (solid) and SFC (dotted). Dashed lines are plotted for $R = 0.23$, and $R = 0.7$, corresponding to buoyancy reversal threshold values.

This hypothetical view of the dynamics of the STCT can be contrasted with cloud-top entrainment instability (CTEI) (Randall 1980; Deardorff 1980; MacVean and Mason 1990; Siems et al. 1990). CTEI predicts a rapid increase in entrainment and entrainment drying, inducing a transition in a matter of an hour or two from stratocumulus to scattered cumulus. Criteria for CTEI are based on the jumps of temperature and mixing ratio across the inversion and, for Siems et al.'s (1990) criterion, the cloud liquid water content. Randall and Deardorff's criteria were based on buoyancy reversal, or the possibility of forming negatively buoyant mixtures of air from within the cloud with air from above the cloud. MacVean and Mason's and Siems et al.'s instability criteria, which are more restrictive, also account for the potential energy that must be expended to allow this mixing to take place.

If the STCT were dominated by CTEI, the distribution of stratocumulus and trade-cumulus clouds in the transition zone should be determined by spatial variations in the jumps of temperature and moisture across the inversion due to varying boundary layer trajectories and upper-air conditions. However, none of the CTEI criteria seem to be skillful in predicting observed cloud amount. Persistent stratocumulus decks in which buoyancy reversal is possible are commonly observed (Kuo and Schubert 1988), while stratocumulus breakup usually occurs well before either of the criteria of MacVean and Mason and Siems et al. are satisfied (Kuo and Schubert 1988; Albrecht 1991; Bretherton et al. 1995). Krueger et al. (1995b) found in their STCT simulations that when stratocumulus clouds were dissipating, negatively buoyant downdrafts were much less vigorous than updrafts, in contradiction to the predictions of CTEI.

We can compare the predictions of CTEI criteria with the stratocumulus breakup in Cbase. Figure 11 plots cloud fraction (SFC) and $R = (C_p\Delta\theta_e)/(L\Delta q_t)$ (MacVean and Mason 1990). The cloud-top jumps of $\Delta\theta_e$ and Δq_t

are taken as differences from 75 m above the inversion to 50 m below the inversion and horizontally averaged over the domain. The CTEI criteria of Randall (1980) and Deardorff (1980) predicts instability when $R > k_2$. Similarly, the buoyancy reversal criterion of MacVean and Mason (1990) is $R > R_c$. (Here, $k_2 \approx 0.23$ and $R_c \approx 0.7$ are thermodynamic parameters that depend weakly on temperature and pressure.) The value of R increases gradually from -0.7 to 0.6 through the simulation, coincident with the steady weakening of the temperature inversion. The decline in SFC begins at 4.5 days, well before R reaches k_2 during day 7. On the other hand, the 6-h time-smoothed AFC (not shown) does not permanently stay below 0.7 until after day 8, well after R reaches k_2. Here, R never reaches R_c. The overall cloudiness in Cbase appears to be much more highly influenced by cumulus clouds than by CTEI. The fractional coverage of stratiform detraining clouds in the later stages of Cbase appears more closely tied to the time elapsed from the previous cumulus outburst than to the mixing properties between the stratocumulus and the air above.

CTEI could be locally enhancing the entrainment around the edges of cumulus clouds with high q_l near the inversion. The analysis given below suggests, though, that the rate of MBL-top entrainment due to the cumulus clouds as they reach the inversion may be more closely tied to their preexisting turbulence generated by buoyancy than by CTEI.

6. Simulation analysis

Results from Cbase can be used to test key predictions of the DIDECUPE model. Both transitional breakup stages (decoupling at 3 days and stratocumulus breakup at 7–8 days) are evident in Cbase. BW97 look at the first of these stages and compare Cbase to mixed-layer model results. Here, we concentrate on testing the proposed mechanism for the second (CUPE) stage.

If entrainment by penetrative convection is important in the CuSc regime, the time variation of cumulus cloud upward mass flux should correlate highly with the amount of entrainment through the inversion. Wang and Lenschow (1995) found some support for this in ASTEX aircraft observations, showing that the penetrative entrainment averaged over an area including a group of cumulus clouds was larger than in a surrounding region of stratocumulus. In Cbase, we can quantify this relation much more precisely. The cumulus mass flux, M_c, is defined here as the upward mass flux of saturated air at the model level closest to $0.75z_i$. This level is chosen so that it is always below the stratocumulus cloud base but always above the cumulus cloud base even when the cumulus layer is relatively shallow. The value of M_c correlates extremely well with the latent heat flux across the same vertical level; this suggests that cumulus clouds are the dominant agents for sustaining the clouds in the upper MBL during this period. Time series of M_c, entrainment rate, and cloud cover for days 5 to 10 of Cbase are plotted in Fig. 12.

The MBL entrainment rate shows large peaks corresponding to brief spikes in cumulus mass flux. Our interpretation is that the cumulus updrafts cause significant entrainment as they collide with and penetrate the inversion. The detraining-outflow phase of the cumulus events also has an impact on the entrainment rate. The detrained stratocumulus ''anvil'' takes 2 or 3 h to decay following the cumulus events, and the longwave cooling at the top of this stratocumulus drives turbulence and further entrainment. Consequently, the entrainment rate often remains much larger than normal until the anvil decays.

The cumulus clouds both moisten the subinversion layer by detrainment of updraft air and dry this layer by penetrative entrainment. The cloud cover sensitively depends on the relative importance of these two effects. A key prediction of DIDECUPE testable in the model is that the ratio of MBL-top entrainment mass flux, M_e, to cumulus mass flux, M_c, increases as the MBL deepens, causing the cloud layer to dry and the stratocumulus cloud to evaporate. We can further test this in the model by correlating the 15-min average time series of M_e and M_c. The maximum correlation is obtained if we lag the entrainment rate by 7.5 min relative to the cumulus mass flux. Since M_c is measured several hundred meters below the inversion height, this delay can be interpreted as the time needed for a cumulus cloud to rise from $0.75z_i$ up to z_i and generate entrainment. A scatterplot of M_e versus M_c with this lag is shown in Fig. 13 for days 5–10 with differing symbols for each simulation day. As expected from Fig. 12, there is an overall correlation between large cumulus mass flux and large entrainment mass flux on each day. There is also a general increase in entrainment mass flux per unit cumulus mass flux, M_e/M_c, the ''cumulus entrainment efficiency,'' as the simulation progresses. To illustrate this, separate least-squares-fit lines are plotted for each day. The increase in the cumulus entrainment efficiency with the increase in MBL depth strongly supports the DIDECUPE picture of penetrative cumulus entrainment.

Table 3 shows the connection between the cumulus entrainment efficiency taken from the best-fit lines of Fig. 13, some bulk properties of the cumulus convection, and the strength of the inversion, for the last five days of Cbase. Tabulated are the 24-h averages of the convective available potential energy (CAPE) for a lifted parcel with thermodynamic properties equal to the average over the lowest three model grid levels, the inversion jump $\Delta\theta_{vl}$ in virtual liquid water potential temperature, and the cloud-layer thickness δz_c. This thickness is defined as the difference between z_i and the lowest model level at which cloud is found. Also tabulated is the maximum updraft speed $w_{\max}$ over the 24-h period, an inverse bulk Richardson number Ri^{-1} (associated with the cumulus updrafts impinging on the inversion, defined and discussed below), and M_e/M_c.

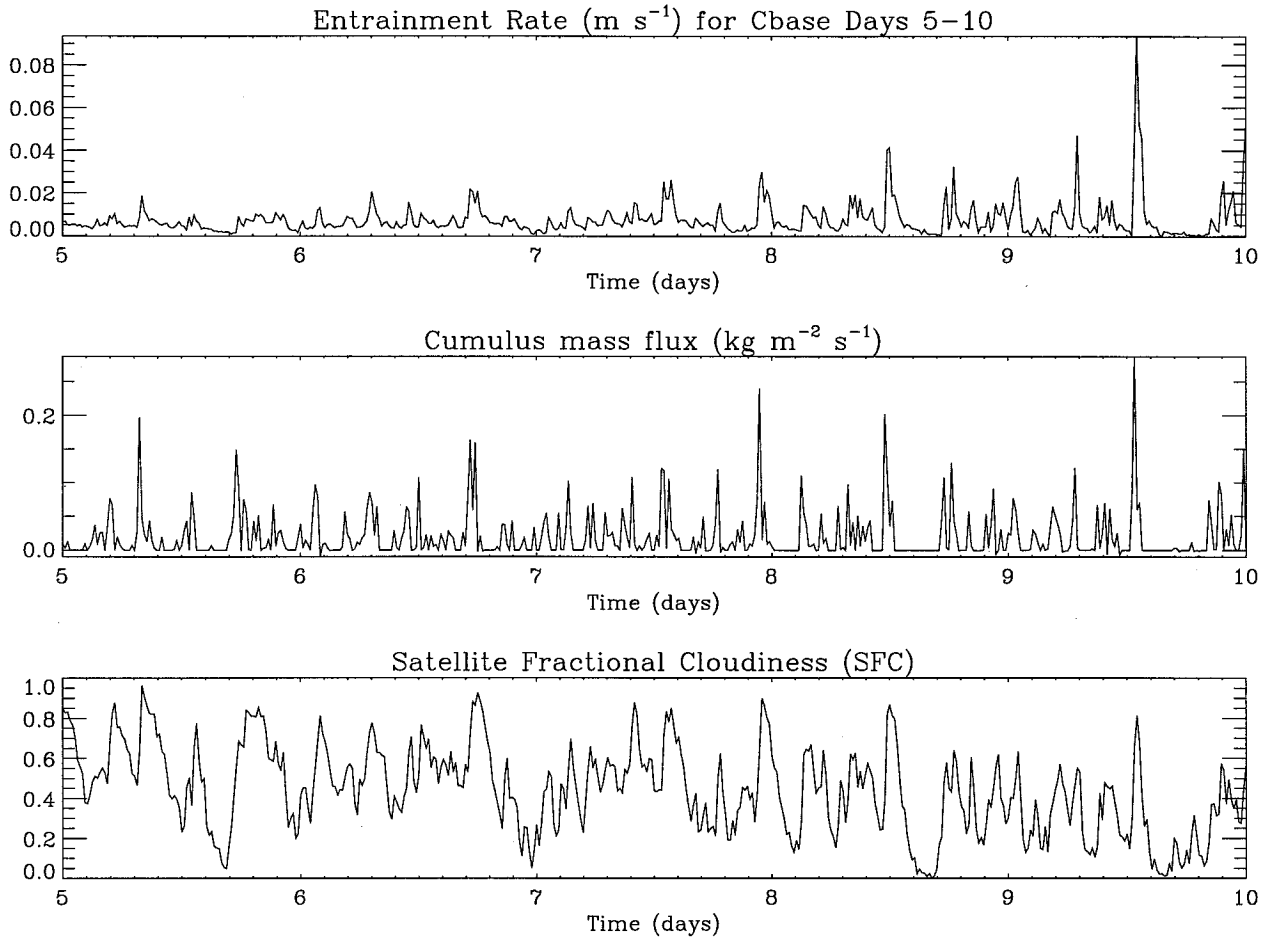

FIG. 12. Time series of Cbase days 5–10: (a) cloud-top entrainment rate, (b) cumulus mass flux at $0.75z_i$ (M_c), (c) satellite fractional cloudiness (SFC).

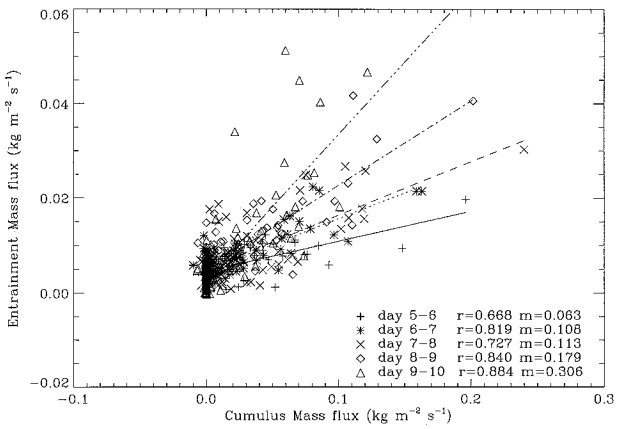

FIG. 13. Scatterplot of M_e vs M_c. The entrainment rate is lagged by 7.5 min relative to the cumulus mass flux. Differing symbols are used for each 24-h period and are given in the legend. Best-fit lines are plotted for days 5–6 (solid), days 6–7 (dotted), days 7–8 (dashed), days 8–9 (dashed–dotted), and days 9–10 (dashed–3-dotted). The correlation coefficient, r, and the slope, m, for each line are tabulated in the legend.

Note that the CAPE in Table 3 is computed using irreversible thermodynamics. The irreversible CAPE is larger than reversible CAPE by about $g\delta z_c\,(q_l)_{\text{avg}}$, where $(q_l)_{\text{avg}}$ is the mean cloud water of the parcel after lifting above the LCL. Given that $(q_l)_{\text{avg}}$ is generally less than 0.7 g kg^{-1}, the difference between irreversible CAPE and reversible CAPE is always less than 10 m^2 s^{-2} and scales linearly with the irreversible CAPE tabulated here.

As expected for cumulus convection, $w_{\max}$ scales approximately as (CAPE)$^{1/2}$ and roughly doubles from days

TABLE 3. CAPE and the entrainment efficiency of cumulus convection for Cbase days 5–10. All of the tabulated quantities are 24-h averages, except w_{max}, which is the maximum w over the 24-h period.

Day	CAPE (m^2 s^{-2})	$w_{\max}$ (m s^{-1})	$\Delta\theta_{vl}$ (K)	δz_c (m)	Ri^{-1}	M_e/M_c
5–6	22.0	2.35	7.08	432	0.22	0.06
6–7	31.9	3.05	6.08	524	0.31	0.11
7–8	39.8	3.68	5.40	641	0.35	0.11
8–9	53.7	4.19	3.61	776	0.39	0.18
9–10	86.9	5.44	3.53	975	0.77	0.31

5–6 to days 9–10. At the same time, the inversion strength halves, also promoting greater cumulus entrainment efficiency. These two effects are actually coupled. The dominant energy balance of a subtropical MBL requires that entrainment warming $w_e\Delta\theta_{vl}$ approximately equal the cumulus-layer integrated radiative cooling (BW97). From Fig. 7d, the latter decreases between 5 and 10 days into Cbase, but only by 30%. The much larger decrease in the inversion strength is a direct consequence of a 50% increase in the overall entrainment rate between days 5 and 10, which in part is related to the increasing cumulus entrainment efficiency.

We now propose a simple parameterization of cumulus entrainment efficiency that uses only parameters that are available from a one-dimensional model of the MBL. We assume that penetrative entrainment due to cumulus updrafts impinging upon the inversion is analogous to entrainment by a turbulent flow through a stratified interface, except that it occurs only over a small areal fraction of the inversion. For entrainment through a stratified interface in a fluid such as air in which the molecular diffusivity and the viscosity are comparable, Turner (1968) found that the ratio of the entrainment rate to a characteristic vertical velocity of the turbulent eddies scales as Ri^{-1}, where Ri is a bulk Richardson number based on the eddy velocity and the buoyancy jump across the interface. For a cumulus cloud, we choose a velocity scale $w_c = (\mathrm{CAPE})^{1/2}$, an eddy length scale equal to the cloud depth δz_c, and the interfacial buoyancy jump is $\Delta b = g\Delta\theta_{vl}/\bar{\theta}$, so

$$\mathrm{Ri} = \Delta b\delta z_c/\mathrm{CAPE}. \tag{14}$$

In cumulus clouds, the motions are predominantly upward, so the cumulus mass flux per unit area scales with the characteristic vertical velocity. Thus, the ratio of the entrained mass flux to the updraft mass flux (the cumulus entrainment efficiency) should also scale as

$$M_e/M_c = A/\mathrm{Ri}, \tag{15}$$

where A is an empirically determined constant of proportionality. This parameterization is supported by our analysis of Cbase. The values of Ri^{-1} and M_e/M_c in Table 3 are nearly proportional, with a best-fit $A = 0.4$. The estimated standard deviation of M_e/M_c from the fit (15) is 0.025.

One implication of (15) is that if parameterizations of shallow cumulus convection are to realistically capture the transitional dynamics associated with the STCT, they should explicitly incorporate some representation of penetrative entrainment by cumuli. For a cumulus parameterization that sets the cloud top to be the level of neutral buoyancy of updraft air, this must be done explicitly by adding an entrainment term of the form (15), which modifies the properties of the updraft air reaching the inversion before it is detrained from the cloud.

Some cumulus parameterizations assume that the cumulus cloud overshoots its level of neutral buoyancy, continuing to entrain during this penetrative phase. These parameterizations automatically produce penetrative entrainment that scales as in (15). For instance, consider a parcel model of a homogeneous cumulus updraft vertically accelerated by its own buoyancy, with a lateral entrainment rate that is independent of height up to the diagnosed cloud top. If such a model is applied to a cumulus cloud impinging on a sharp inversion, the cloud top will be a distance $O(w_c^2/\Delta b) = O(\mathrm{Ri}^{-1}\delta z_c)$ above the level of neutral buoyancy. Hence, a fraction $O(\mathrm{Ri}^{-1})$ of the lateral entrainment occurs above the inversion, after which this entrained air is brought back down into the boundary layer. This has exactly the effect given in (15), though it may not produce a reasonable value of the constant A without tuning.

A related uncertainty is the simulated entrainment rate at stratocumulus cloud top. A recent experiment (to be reported on in a forthcoming paper by M. MacVean et al.) investigated differences in entrainment rate between different models in an idealized smoke-cloud simulation. This experiment showed a significant difference in the relation between buoyancy flux and entrainment rate between two-dimensional and three-dimensional simulations, as well as significant sensitivity to vertical resolution. We do not believe that these sensitivities will have a large effect on the overall entrainment rate through the stratocumulus cloud top, because of the dominant balance between radiative cooling and entrainment warming, which places strong constraints on the entrainment rate. Biases or errors in entrainment rate will affect the quasi-steady-state liquid water path and buoyancy fluxes in stratocumulus but should not qualitatively change the STCT.

7. Sensitivity simulations

In the Cwide simulation, we attempt to assess whether the restricted domain width is affecting the observed fractional cloudiness. In a wide domain, one might obtain a widely spaced field of cumulus clouds with only slight high frequency variations in the horizontally averaged cloud properties and fluxes. In a domain much narrower than the natural spacing between cumuli such as used in Cbase, the same boundary conditions would produce intermittent bursts of convection. This may affect the cloudiness in our simulations, particularly in the cumulus under stratocumulus regime, by altering the mean characteristics of the detrained stratocumulus anvils from cumulus clouds.

We extend the width of the model domain by a factor of three to 12 km in Cwide while maintaining the grid resolution of Cbase to assess whether the restricted domain width is affecting the observed fractional cloudiness. Cwide is started from a motionless state using the mean sounding at 72 h in Cbase and run for 4 days with boundary conditions identical to those of Cbase from day 3 to day 7.

Most of the MBL statistics such as surface fluxes and

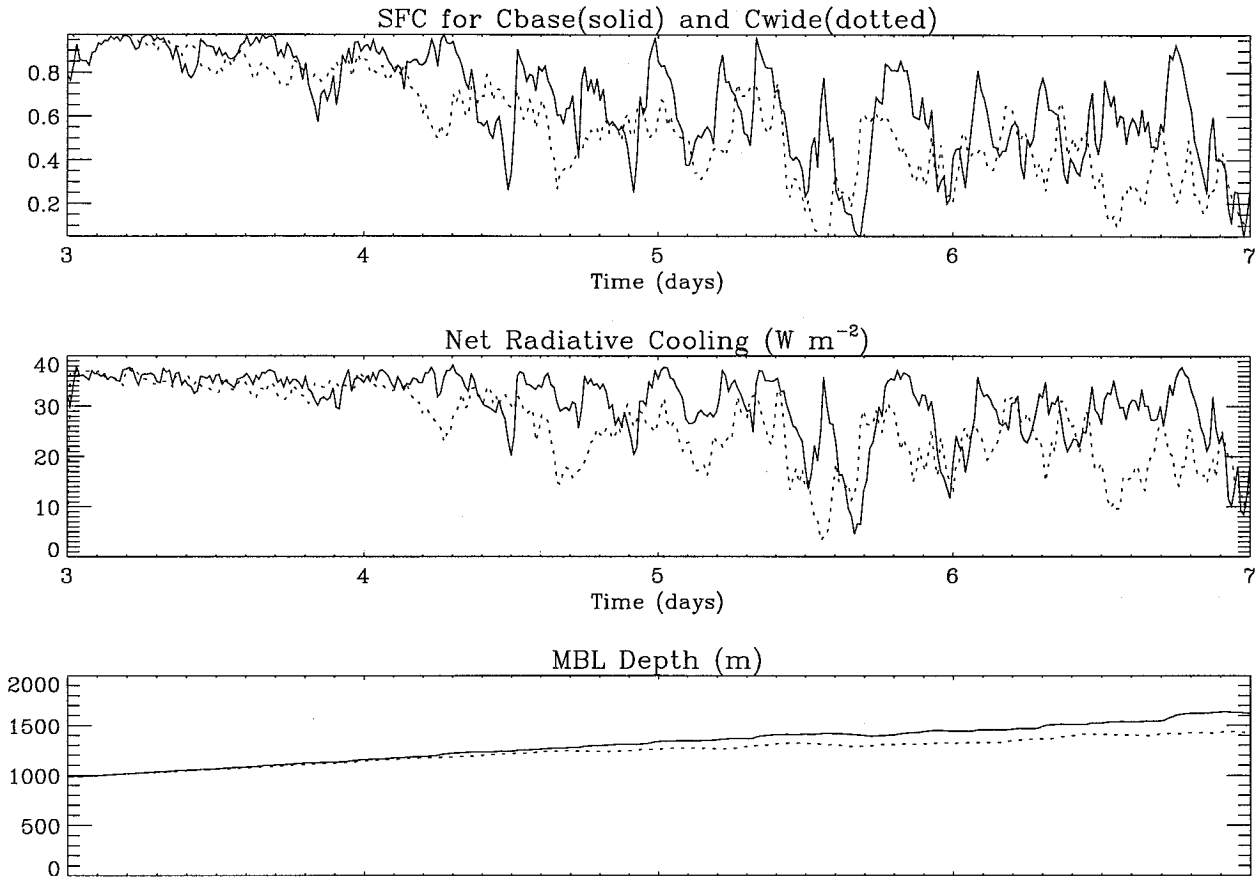

FIG. 14. Time series of Cbase days 3–7 (solid) and Cwide (dotted): (a) SFC, (b) net MBL radiative cooling, (c) mean MBL depth.

mean resolved TKE are more smoothly varying in Cwide than in Cbase but have nearly identical mean behavior. The mean soundings in the MBL are also nearly identical. However, Cwide has three to four convective cells in the MBL while Cbase has only one or two. This produces a better "ensemble" average of convection than Cbase, but the domain is still not wide enough to completely represent the mesoscale structures frequently seen in stratocumulus and CuSc. Like Cbase, the cumulus convection in Cwide is not stationary; there are no long-lived cumulus "towers," which continuously convect into the overlying stratus. The largest cumulus clouds survive for a couple of hours.

Some statistics comparing the two runs are shown in Fig. 14. The average cloud fraction (SFC) is about 0.1 lower in Cwide, which results in 20% lower average MBL radiative cooling after the first 20 h. Related to these differences, the final MBL depth in Cwide is about 150 m less than that in Cbase. Overall entrainment rate is about 1 mm s^{-1} lower in Cwide than in Cbase.

It appears that the lower fractional cloudiness in Cwide is reducing the entrainment because of the diminished longwave cooling. The cause of the lower fractional cloudiness itself may be due to the larger domain in which detrained stratus can spread and dissipate before being replenished by more cumulus convection. The effects of cumulus penetrative entrainment in Cwide are similar to those in Cbase, with the strongest cumulus mass fluxes causing peaks in entrainment and significant drying of the upper MBL.

The sporadic behavior of the fractional cloudiness and other statistics in the narrow domain is also manifested in tests we have performed using different initial random seeds in Cbase. All the runs with different random seeds show the same mean trends and extremely similar bulk boundary layer properties at various times. However, the fractional cloudiness and the timing of cumulus convection can vary significantly between days and between differently seeded runs.

The interpretation of two-dimensional simulations of three-dimensional processes should be made with some caution. Two-dimensional simulations produce anomalous upscale transport of TKE producing significant mean boundary-layer vertical shear and coherent roll-like structures, which are not necessarily realistic. The mean shear that develops in Cbase, Dbase, and Cwide (sometimes as large as 0.01 s^{-1}) does not strongly affect the nature of the convection because the buoyant production of TKE is still much larger than shear production. Sensitivity simulations we have performed with

much less shear do not vary substantially with ones presented here. Ideally, however, simulations involving mixed layers should have much smaller vertical wind shear.

A comparison of numerous two-dimensional and three-dimensional simulations of an identical stratocumulus-topped boundary layer by Moeng et al. (1996) showed significant differences in vertical momentum fluxes, velocity variances, and TKE between two-dimensional and three-dimensional simulations. These characteristics of two-dimensional simulations can be expected to affect the timing of decoupling and the nature of the simulated cumulus convection. Despite these differences, the mean thermodynamic profiles and scalar fluxes are quite similar between the two types of model simulations.

8. Conclusions

An idealized stratocumulus to trade cumulus transition has been simulated using a Lagrangian approach and a 2D ERM model. We have proposed a hypothesis, DIDECUPE, relating the cloudiness transition to changes in boundary layer vertical structure that lead to increasing penetrative entrainment by cumulus clouds as the SST rises. The diurnal cycle of radiation strongly modulates fractional cloudiness but does not affect the systematic changes in cloud amount, type, and MBL structure associated with the transition. At the early stages of the simulations the boundary layer is shallow and well mixed, with solid stratocumulus covering the domain. As the SST rises relative to the above-inversion air, the boundary layer deepens. This deepening is associated with increased latent heat fluxes that induce decoupling and lead to a change in the convective structure of the MBL. The boundary layer vertical moisture transport becomes dominated by strong cumuliform updrafts covering a much smaller horizontal area than the downdrafts. This results in vertical stratification of q_t in the upper MBL and a cloud regime of cumulus rising into stratocumulus. The stratocumulus cover remains nearly solid except during the afternoons of the diurnally varying simulation, where solar absorption promotes stratocumulus dissipation. As long as the stratocumulus clouds persist, the vertical stratification of θ_l remains weak.

As the SST rises and the boundary layer deepens, the cumulus clouds become more energetic and entrain significant amounts of dry air from above the inversion. The air they detrain contains less liquid water, the resulting stratocumulus become thin and patchy, and the MBL takes on the characteristics of the trade-cumulus boundary layer.

Many important issues remain to be investigated. The CuSc regime appears to require advection from cold to warm SST, since the convection in the subcloud layer is driven exclusively by surface buoyancy fluxes promoted by air colder than the underlying ocean surface. In the western branch of the trades, where the air flows from warm to cold SST, the MBL evolution is probably quite different and is much less well studied. Also, the climatological decrease in subsidence, which was neglected in these simulations, has a significant effect on boundary layer depth and therefore could influence the timing of decoupling and the nature of the STCT.

Boundary layer life cycles in a typical midlatitude baroclinic wave might also usefully be studied with a Lagrangian ERM, though data for comparison is sparse.

The sensitivity of the stratocumulus to trade-cumulus transition to changes in the rate of rise of SST, the droplet concentration or drizzle parameterization, local changes in the lower-tropospheric stability, subsidence specification, and the wind speed will be explored in a forthcoming paper.

Acknowledgments. This work was supported by ONR Grant N00014-90-J-1136, NASA Grant NAG1-1711, and an NSF Graduate Fellowship awarded to M. C. Wyant. The thorough reviews and comments of Doug Lilly and two anonymous reviewers helped improve this paper.

APPENDIX

Additional Model Physics and Parameterizations

a. Numerics

The model equations are discretized in flux form (i.e., multiplied by $\bar{\rho}$) on a rectangular grid with the velocities staggered a half-grid spacing in their respective directions, using second-order accurate, conservative finite differencing. The momentum equations are advanced using leapfrog-trapezoidal time differencing. Scalar advection follows Smolarkiewicz (1984). Flux limiting (Smolarkiewicz and Grabowski 1990) ensures monotonicity of both scalar and momentum advection. In practice, our scheme remains stable up to Courant numbers of magnitude 0.7. The Poisson equation for the pressure is solved using a discrete fast Fourier transform in the horizontal and a tridiagonal matrix solver in the vertical.

b. Condensation

The cloud water mixing ratio at each grid point is computed assuming no water vapor supersaturation, and the pressure perturbations from p_{env} are thermodynamically negligible (Clark and Farley 1984):

$$q_l = \begin{cases} q_t - q_{\text{sat}}(T, p_{\text{env}}), & q_t > q_{\text{sat}} \\ 0, & q_t < q_{\text{sat}}, \end{cases} \tag{A1}$$

where q_{sat} is the saturation vapor mixing ratio. The value of q_{sat} is evaluated from the Clausius–Clapeyron relation using the following approximate expressions:

$$e_s(T) = e_0 \exp\left[-\frac{L}{R_v}\left(\frac{1}{T} - \frac{1}{T_0}\right)\right],$$

$$q_{\text{sat}}(T, p) = \frac{R_d}{R_v} \cdot \frac{e_s(T)}{p}, \tag{A2}$$

where $e_0 = 610.78$ Pa and $T_0 = 273.16$ K. To solve these equations q_{sat} is written in terms of θ_l and q_l and substituted into Eq. (A1). The resulting equation is then solved at each grid point using four iterations of Newton's method, following Clark and Farley (1984).

c. Turbulence

The model uses a first-order subgrid-scale turbulence closure (Smagorinsky 1963; Lilly 1962) modified to account for the effects of evaporation following Mason (1985). The eddy viscosity, K_M, is computed from the Richardson number, Ri, and the amplitude of the deformation tensor, $|\text{def}|$:

$$K_M = \begin{cases} (C_s\Delta)^2|\text{def}|\sqrt{1 - \text{Ri}}, & \text{Ri} < 0 \\ (C_s\Delta)^2|\text{def}|(1 - \beta\text{Ri})^2, & 0 < \text{Ri} < 1/\beta \\ 0, & 1/\beta < \text{Ri}, \end{cases}$$

$$|\text{def}| = \sqrt{\frac{1}{2}D_{ij}D_{ij}}. \tag{A3}$$

Here, $\beta = 3$, $C_s = 0.19$, and $\Delta = (\Delta x \cdot \Delta y \cdot \Delta z)^{1/3}$, where $(\Delta x, \Delta y, \Delta z)$ is the size of a grid box. The Richardson number is computed using the method of Mason (1985) in which the potential effects of buoyancy reversal (Randall 1980; Deardorff 1980) between two vertically separated grid points are accounted for. From the eddy viscosity for momentum, K_m, we calculate the eddy viscosity for heat and moisture by multiplying by a turbulent Prandtl number, Pr, set to 0.4:

$$K_H = K_Q = \text{Pr}K_M. \tag{A4}$$

These eddy viscosities are used in the momentum and scalar Eqs. (3)–(7).

d. Radiation

The radiative fluxes in each vertical column of the model domain are found using two-stream schemes from Herman and Goody (1976) for both longwave and shortwave radiation. The single-band effective transmissivity longwave scheme includes the radiative effects of water vapor and droplets, but not CO_2 or O_3. The transmissivities of water vapor Tr_v and liquid water Tr_l used in the scheme are

$$\text{Tr}_v = (1 + 0.8P_v)^{-1/2}, \tag{A5}$$

$$\text{Tr}_l = \exp(-156P_l), \tag{A6}$$

where P_v and P_l are vertical water vapor and liquid water paths (in kg m^{-2}) without any pressure corrections added.

The scheme was tested against a more detailed multiband scheme of Roach and Slingo (1979) using idealized stratocumulus-capped mixed-layer soundings with a fixed inversion height of 800 m, surface air and sea temperatures both 291 K, isothermal above-inversion temperature of 291 K, above-inversion mixing ratio of 4 g kg^{-1} up to a domain top at 1000 m, and specified midlatitude summertime climatological soundings above 1000 m. The mixed-layer mixing ratio was varied to change the cloud depth and hence cloud liquid water path. Very close agreement of overall radiative flux divergence through the cloud layer was found between the two schemes. The shortwave scheme was modified to a three-band scheme with spectral fractions (0.77, 0.15, 0.08) and vapor absorptivities $k_v = (0.0005, 0.005, 0.255)$ (m^2 kg^{-1}) in the three bands. The droplet scattering coefficient in all bands is $k_s = 6/(4\pi r\rho_l)$, the large-radius Mie limit for nonabsorptive drops. The droplet absorption coefficients are $k_a = (0, 11.54, 11.54)r_{\text{eff}}^{-0.55}$ (m^2 kg^{-1}), where r_{eff} is the effective radius in μm. The effective radius at all cloudy levels in a column is defined as 0.7 times the maximum mean drop radius in the column. This is chosen to weight the effective radius towards the levels a little below cloud top because of their importance in scattering. The absorption coefficients have been modified from Herman and Goody (1976) to provide cloud heating rates in good agreement with the Slingo and Schrecker (1982) scheme for idealized stratocumulus clouds with the sun at zenith. A good fit for the mixed-layer test case mentioned above has been achieved over the entire range of cloud depths, but the albedo is consistently lower than in the Slingo–Schrecker scheme. Solar radiation is treated as diffuse, which also reduces the albedo away from zenith. However, for this study, the heating (which feeds back on the cloud dynamics) is much more important than the albedo (which is important more for observational comparisons).

To reduce the computational overhead, the radiation for the entire model domain is only computed once every 5 min of simulation time. However, in every grid box the value of q_l is monitored to see if new cloud water appears or if all of the existing cloud water evaporates between time steps. If any grid points in an individual column satisfy either of these conditions, the radiative fluxes for that column are recomputed immediately.

e. Microphysics

HUSCI uses a Kessler-type bulk warm microphysics scheme that is a hybrid of schemes in Liou and Ou (1989), Chen and Cotton (1987), and Baker (1993). The effect of gravitational settling of cloud water, q_l, representing drops smaller than about 40 μm, is neglected in the Eq. (6) for q_t. The second drop category, rain-

water, q_r, is allowed to gravitationally settle and assumed to have a Marshall–Palmer distribution governed by a single drop size parameter. From this distribution, a mass-weighted effective fall speed is computed from which the flux of q_r due to gravitational settling is calculated.

Rainwater is generated through autoconversion and accretion and can evaporate in subsaturated air. The parameterized autoconversion rate, P_1, the accretion rate P_2, evaporation rate, E, and the rainwater precipitation flux, F_p, enter the model equations in the following source terms:

$$\left(\frac{\partial q_t}{\partial t}\right)_{\text{microphysics}} = -(P_1 + P_2 - E), \quad \text{(A7)}$$

$$\left(\frac{\partial q_r}{\partial t}\right)_{\text{microphysics}} = P_1 + P_2 - E - \frac{1}{\bar{\rho}}\frac{\partial F_P}{\partial z}, \quad \text{(A8)}$$

$$\left(\frac{\partial \theta_l}{\partial t}\right)_{\text{microphysics}} = \frac{L}{C_p \Pi_{\text{env}}}(P_1 + P_2 - E). \quad \text{(A9)}$$

The microphysical source terms are functions of q_l, q_r, and the relative humidity (RH).

Autoconversion is the creation of q_r from q_l through the collisions of cloud water drops. Following Liou and Ou (1989) and others, the autoconversion rate based on collision theory is given by

$$P \approx q_l \bar{E}_1 \int \pi r^2 V(r) n(r) dr = \pi \bar{E}_1 C_1 N \bar{r}_w^4 q_l. \quad \text{(A10)}$$

Here, $\overline{E}_1 = 0.55$ is a mean autoconversion efficiency parameter, $V(r) = C_1 r^2$ is the terminal fall speed of a drop of radius r ($C_1 = 1.19 \times 10^8$ m^{-1} s^{-1}), $n(r)$ is the drop size distribution, $N = \int n(r)\, dr$ is the total cloud water drop concentration, and $\bar{r}_w = [1/N \int r^4 n(r)\, dr]^{1/4}$ is a fourth-moment drop radius. This approximate collision kernel is based on a simple model of large drops capturing smaller drops that have negligible terminal fall speeds. We assume that all cloud condensation nuclei (CCN) below some fixed supersaturation are activated in cloud, one to a drop, so that N is identical to this specified CCN concentration.

Instead of fixing the parameter $\bar{r}_w$ as was done by Liou and Ou, we follow the method of Chen and Cotton (1987) and Baker (1993) and estimate $\bar{r}_w$ from the cloud water mixing ratio assuming uniform drop size:

$$\bar{r}_w = \left(\frac{1}{N}\frac{3}{4\pi}\frac{\bar{\rho}}{\rho_l} q_l\right)^{1/3}. \quad \text{(A11)}$$

Here, ρ_l is the density of liquid water and $\bar{\rho}$ is determined from the anelastic base state. If the droplet radius is less than 10 μm, we multiply the autoconversion rate by the factor $(\bar{r}_w/10\ \mu m)^3$, so that the autoconversion rate diminishes smoothly but rapidly to zero for small q_l or large N. Baker (1993) and Austin et al. (1995) point out that Eq. (A10) still gives autoconversion rates too high compared to better resolved microphysical schemes and observations, so we attempt to account for this using a multiplicative constant $\alpha = 0.5$ in our autoconversion rate. The final expression for autoconversion rate is, thus,

$$P_1 = \pi \alpha \bar{E}_1 C_1 N \bar{r}_w^4 \chi(\bar{r}_w) q_l,$$

$$\chi(\bar{r}_w) = \begin{cases} 1, & \bar{r}_w \geq 10\ \mu m \\ (\bar{r}_w/10\ \mu m)^3, & \bar{r}_w < 10\ \mu m, \end{cases} \quad \text{(A12)}$$

which is used in conjunction with Eq. (A11). If (A11) is substituted into (A12), it is easily shown that for $\bar{r}_w \geq 10\ \mu m$, $P_1 \propto N^{-1/3} q_l^{7/3}$, so that a factor of 8 increase in CCN concentration produces a halving of the autoconversion rate. For $\bar{r}_w \leq 10\ \mu m$ (which for $N = 50$ cm^{-3} approximately corresponds to $q_l \leq 0.2$ g kg^{-1}), $P_1 \propto N^{-4/3} q_l^{10/3}$ so there is a much stronger dependence of autoconversion on CCN concentration.

The rainwater component of the microphysics is based the free parameter r_m, the mass-weighted drop radius. The raindrops are assumed to follow a Marshall–Palmer type rainwater distribution given by

$$n(r) = n_0 \exp(-r/r_m), \quad \text{(A13)}$$

where n_0 and r_m are free parameters and $n(r)$ is the number of droplets with radius between r and $r + dr$. Tripoli and Cotton (1980) allow n_0 to vary with the rainwater mixing ratio due to raindrop breakup effects, but here $n_0 = 8 \times 10^6$ m^{-4} is held fixed because the rainwater contents in the stratocumulus and trade-cumulus simulations are small. An expression for r_m can be derived by integrating (A13) over all r;

$$r_m = \left(\frac{\bar{\rho} q_r}{8\pi \rho_l n_0}\right)^{1/4}. \quad \text{(A14)}$$

To determine the precipitation flux of a given raindrop distribution, we use the fall speed parameterization from Rogers and Yau (1989) for drops smaller than 600μm:

$$V = C_1 r^2 \qquad r < 40\ \mu\text{m},$$

$$V = C_2 r \qquad r \geq 40\ \mu\text{m}, \quad \text{(A15)}$$

where $C_1 = 1.19 \times 10^8$ m^{-1} s^{-1} and $C_2 = 8.0 \times 10^3$ s^{-1}. The precipitation flux, F_P, is computed by integrating the fall speed over the drop size distribution (A13) and neglecting the small C_1 term:

$$F_P = -4\bar{\rho} C_2 r_m q_r. \quad \text{(A16)}$$

Accretion is the collection of cloud water drops by rainwater drops. Following Liou and Ou (1989), we presume the cloud water drops are stationary and apply Eq. (A10) using the large drop terminal fall speed in (A15) and a collection efficiency $\overline{E}_2 = 1.0$. This gives an approximate accretion rate P_2,

$$P_2 \approx q_l \bar{E}_2 \int \pi r^2 C_2 r n_0 \exp(-r/r_m)\, dr = -\frac{3}{16}\frac{\bar{E}_2 F_P q_c}{\rho_l r_m}. \quad \text{(A17)}$$

The evaporation rate is derived using the droplet evaporation expression from Rogers and Yau (1989, 102), integrated over the Marshall–Palmer distribution:

$$E = \begin{cases} \dfrac{8\pi n_0 (1 - RH)}{\bar{\rho}\quad (A + B)}\left[0.39 r_m^3 + 0.40\left(\dfrac{\bar{\rho} C_2}{\mu}\right)^{1/2} r_m^3\right], & \text{RH} < 1.0 \\ 0, & \text{RH} = 1.0 \end{cases}$$

$$A = \frac{L^2}{K R_v T_{\text{env}}^2}, \qquad B = \frac{R_v T_{\text{env}}}{D_{\text{vap}} e_s(T_{\text{env}})}. \quad \text{(A18)}$$

Here, RH $= q_v/q_{\text{sat}}$ is the relative humidity, $e_s(T)$ is the saturation vapor pressure, $\mu = 1.766 \times 10^{-5}$ kg m^{-1} s^{-1} is the dynamic viscosity of air, $K = 2.48 \times 10^{-2}$ J m^{-1} s^{-1} K^{-1} is the coefficient of thermal conductivity of air, and $D_{\text{vap}} = 2.36 \times 10^{-5}$ m^2 s^{-1} is the coefficient of vapor diffusion.

f. Sponge layer

To eliminate the effects of gravity wave reflections, we use a sponge layer in the upper part of the domain similar to Chlond (1992). Rayleigh-damping terms are added to the momentum and θ_l equations as follows:

$$\left(\frac{\partial \mathbf{u}}{\partial t}\right)_{\text{sponge}} = -\nu(\mathbf{u} - \mathbf{u}_g),$$

$$\left(\frac{\partial \theta_l}{\partial t}\right)_{\text{sponge}} = -\nu(\theta_l - \langle\theta_l\rangle). \quad \text{(A19)}$$

The Rayleigh damping coefficient profile is given by

$$\nu = \begin{cases} \nu_0 \sin^2\left(\dfrac{\pi}{2}\dfrac{z - z_s}{L_z - z_s}\right), & z > z_s \\ 0, & z < z_s, \end{cases} \quad \text{(A20)}$$

where $\nu_0 = (300\ \text{s})^{-1}$ is the maximum damping coefficient, L_z is the height of the domain, and z_s is the specified minimum height of the sponge.

REFERENCES

Albrecht, B. A., 1991: Fractional cloudiness and cloud-top entrainment instability. *J. Atmos. Sci.,* **48,** 1519–1525.

——, A. K. Betts, W. H. Schubert, and S. K. Cox, 1979: A model of the thermodynamic structure of the trade-wind boundary layer: Part I. Theoretical formulation and sensitivity tests. *J. Atmos. Sci.,* **36,** 90–98.

——, D. A. Randall, and S. Nicholls, 1988: Observations of marine stratocumulus clouds during FIRE. *Bull. Amer. Meteor. Soc.,* **69,** 618–626.

——, C. S. Bretherton, D. Johnson, W. H. Schubert, and A. S. Frisch, 1995: The Atlantic Stratocumulus Transition Experiment (ASTEX). *Bull. Amer. Meteor. Soc.,* **76,** 889–903.

Austin, P., Y. Wang, R. Pincus, and V. Kujala, 1995: Precipitation in stratocumulus cloud: Observational and modeling results. *J. Atmos. Sci.,* **52,** 2329–2352.

Baker, M. B., 1993: Variability in concentrations of cloud concentration nuclei in the marine cloud-topped boundary layer. *Tellus,* **45B,** 458–472.

Betts, A. K., P. Minnis, W. Ridgway, and D. F. Young, 1992: Integration of satellite and surface data using a radiative-convective oceanic boundary-layer model. *J. Appl. Meteor.,* **31,** 340–350.

Bougeault, P., 1985: The diurnal cycle of the marine stratocumulus layer: A higher order model study. *J. Atmos. Sci.,* **42,** 2826–2843.

Bretherton, C. S., 1992: A conceptual model of the stratocumulus-trade-cumulus transition in the subtropical oceans. *Proc. 11th Int. Conf. on Clouds and Precipitation,* Vol. 1, Montreal, PQ, Canada, Int. Comm. on Clouds and Precipitation and Int. Assoc. of Meteor. and Atmos. Phys., 374–377.

——, 1993: Understanding Albrecht's model of trade cumulus cloud fields. *J. Atmos. Sci.,* **50,** 2264–2283.

——, and R. Pincus, 1995: Cloudiness and marine boundary layer dynamics in the ASTEX Lagrangian experiments. Part I: Synoptic setting and vertical structure. *J. Atmos. Sci.,* **52,** 2707–2723.

——, and M. C. Wyant, 1997: Moisture transport, lower tropospheric stability, and decoupling of cloud-topped boundary layers. *J. Atmos. Sci.,* **54,** 184–167.

——, P. Austin, and S. Siems, 1995: Cloudiness and marine boundary layer dynamics in the ASTEX Lagrangian experiments. Part II: Cloudiness, drizzle, surface fluxes, and entrainment. *J. Atmos. Sci.,* **52,** 2724–2735.

Chen, C., and W. R. Cotton, 1987: The physics of the marine stratocumulus-capped mixed layer. *J. Atmos. Sci.,* **44,** 2951–2977.

Chlond, A., 1992: Three-dimensional simulation of cloud street development during a cold air outbreak. *Bound.-Layer Meteor.,* **58,** 161–200.

Clark, T. L., and W. R. Farley, 1984: Severe downslope windstorm calculations in two and three spatial dimensions using anelastic grid nesting: A possible mechanism for gustiness. *J. Atmos. Sci.,* **41,** 329–350.

Deardorff, J. W., 1980: Cloud top entrainment instability. *J. Atmos. Sci.,* **37,** 131–147.

Hartmann, D. L., M. E. Ockert-Bell, and M. L. Michelsen, 1992: The effect of cloud type on the earth's energy balance. *J. Climate,* **5,** 1281–1304.

Herman, G., and R. Goody, 1976: Formation and persistence of summertime arctic stratus clouds. *J. Atmos. Sci.,* **33,** 1537–1553.

Klein, S. A., and D. L. Hartmann, 1993: The seasonal cycle of low stratiform clouds. *J. Climate,* **6,** 1587–1606.

——, ——, and J. R. Norris, 1995: On the relationships among low cloud structure, sea surface temperature, and atmospheric circulation in the summertime northeast Pacific. *J. Climate,* **8,** 1140–1155.

Kogan, Y. L., M. P. Khairoutdinov, D. K. Lilly, Z. N. Kogan, and Q. Liu, 1995: Modeling of stratocumulus cloud layers in a large eddy simulation model with explicit microphysics. *J. Atmos. Sci.,* **52,** 2923–2940.

Krueger, S. K., and A. Bergeron, 1994: Modeling the trade cumulus boundary layer. *Atmos. Res.,* **33,** 169–192.

——, G. T. McLean, and Q. Fu, 1995a: Numerical simulation of the stratus-to-cumulus transition in the subtropical marine boundary layer. Part I: Boundary-layer structure. *J. Atmos. Sci.,* **52,** 2839–2850.

——, ——, and ——, 1995b: Numerical simulation of the stratus-to-cumulus transition in the subtropical marine boundary layer.

Part II: Boundary-layer circulation. *J. Atmos. Sci.,* **52,** 2851–2868.

Kuo, H.-C., and W. H. Schubert, 1988: Stability of cloud-topped mixed layers. *Quart. J. Roy. Meteor. Soc.,* **114,** 887–916.

Lilly, D. K., 1962: On the numerical simulation of buoyant convection. *Tellus,* **14,** 148–172.

——, 1968: Models of cloud-topped mixed layers under a strong inversion. *Quart. J. Roy. Meteor. Soc.,* **94,** 292–309.

Liou, K. N., and S. C. Ou, 1989: The role of cloud microphysical processes in climate: An assessment from a one-dimensional perspective. *J. Geophys. Res.,* **94,** 8599–8607.

MacVean, M. K., 1993: A numerical investigation of the criterion for cloud-top entrainment instability. *J. Atmos. Sci.,* **50,** 2481–2495.

——, and P. J. Mason, 1990: Cloud-top entrainment instability through small-scale mixing and its parameterization in numerical models. *J. Atmos. Sci.,* **47,** 1012–1030.

Mason, P. J., 1985: A numerical study of cloud streets in the planetary boundary layer. *Bound.-Layer Meteor.,* **32,** 281–304.

——, and R. I. Sykes, 1982: A two-dimensional numerical study of horizontal roll vortices in an inversion-capped planetary boundary layer. *Quart. J. Roy. Meteor. Soc.,* **108,** 801–823.

Minnis, P., P. W. Heck, D. F. Young, C. W. Fairall, and J. B. Snider, 1992: Stratocumulus cloud properties derived from simultaneous satellite and island-based instrumentation during FIRE. *J. Appl. Meteor.,* **31,** 317–339.

Moeng, C.-H., 1986: Large-eddy simulation of a stratus-topped boundary layer. Part I: Structure and budgets. *J. Atmos. Sci.,* **43,** 2886–2900.

——, D. H. Lenschow, and D. A. Randall, 1995: Numerical investigations of the roles of radiative and evaporative feedbacks in stratocumulus entrainment and breakup. *J. Atmos. Sci.,* **52,** 2869–2883.

——, and Coauthors, 1996: Simulation of a stratocumulus-topped planetary boundary layer: Intercomparison among different numerical codes. *Bull. Amer. Meteor. Soc.,* **77,** 261–278.

Neiburger, M., D. S. Johnson, and C.-W. Chien, 1961: *The Inversion over the Eastern North Pacific Ocean.* Vol. 1, *Studies of the Structure of the Atmosphere over the Eastern Pacific Ocean in Summer,* University of California Press, 94 pp.

Nicholls, S., 1984: The dynamics of stratocumulus: Aircraft observations and comparisons with a mixed layer model. *Quart. J. Roy. Meteor. Soc.,* **110,** 783–820.

Ogura, Y., and N. Phillips, 1962: Scale analysis of deep and shallow convection in the atmosphere. *J. Atmos. Sci.,* **19,** 173–179.

Rand, H. A., 1995: Mesoscale dynamics of the marine atmospheric boundary layer. Ph.D. thesis, University of Washington, 136 pp.

Randall, D. A., 1980: Conditional instability of the first kind upside-down. *J. Atmos. Sci.,* **37,** 125–130.

Riehl, H., T. C. Yeh, J. S. Malkus, and N. E. LaSeur, 1951: The northeast trade of the Pacific Ocean. *Quart. J. Roy. Meteor. Soc.,* **77,** 598–626.

Roach, W. T., and A. Slingo, 1979: A high resolution infrared radiative transfer scheme to study the interaction of radiation with cloud. *Quart. J. Roy. Meteor. Soc.,* **105,** 603–614.

Rogers, R. R., and M. K. Yau, 1989: *A Short Course in Cloud Physics.* 3d ed. Pergamon Press, 293 pp.

Schubert, W. H., J. S. Wakefield, E. J. Steiner, and S. K. Cox, 1979: Marine stratocumulus convection. Part II: Horizontally inhomogeneous solutions. *J. Atmos. Sci.,* **36,** 1308–1324.

Siebesma, A. P., and J. W. M. Cuijpers, 1995: Evaluation of parametric assumptions for shallow cumulus convection. *J. Atmos. Sci.,* **52,** 650–666.

Siems, S. T., and C. S. Bretherton, 1992: A numerical investigation of cloud-top entrainment instability and related investigations. *Quart. J. Roy. Meteor. Soc.,* **118,** 787–818.

——, ——, M. B. Baker, S. Shy, and R. E. Breidenthal, 1990: Buoyancy reversal and cloud-top entrainment instability. *Quart. J. Roy. Meteor. Soc.,* **116,** 705–739.

Slingo, A., and H. M. Schrecker, 1982: On the shortwave radiative properties of stratiform water clouds. *Quart. J. Roy. Meteor. Soc.,* **108,** 407–426.

Smagorinsky J., 1963: General circulation experiments with the primitive equations. Part I: The basic experiment. *Mon. Wea. Rev.,* **91,** 99–164.

Smolarkiewicz, P. K., 1984: A fully multidimensional positive definite advection transport algorithm with small implicit diffusion. *J. Comput. Phys.,* **54,** 325–362.

——, and W. W. Grabowski, 1990: The multidimensional positive definite advection transport algorithm: Nonoscillatory option. *J. Comput. Phys.,* **86,** 355–375.

Sommeria, G., 1976: Three-dimensional simulation of turbulent processes in an undisturbed trade wind boundary layer. *J. Atmos. Sci.,* **33,** 216–241.

Soong, S.-T., and Y. Ogura, 1980: Response of tradewind cumuli to large-scale processes. *J. Atmos. Sci.,* **37,** 2035–2050.

Stevens, B., G. Feingold, W. R. Cotton, and R. L. Walko, 1996: Elements of the microphysical structure of numerically simulated nonprecipitating stratocumulus. *J. Atmos. Sci.,* **53,** 980–1006.

Sykes, R. I., W. S. Lewellen, and D. S. Henn, 1988: A numerical study of the development of cloud street spacing. *J. Atmos. Sci.,* **45,** 2556–2569.

Tiedtke, M., W. A. Heckley, and J. Slingo, 1988: Tropical forecasting at ECMWF: The influence of physical parameterization on the mean structure of forecasts and analyses. *Quart. J. Roy. Meteor. Soc.,* **114,** 639–644.

Tripoli, G. J., and W. R. Cotton, 1980: A numerical investigation of several factors contributing to the observed variable intensity of deep convection over south Florida. *J. Appl. Meteor.,* **19,** 1037–1063.

Turner, J. S., 1968: The influence of molecular diffusivity on turbulent entrainment across a density interface. *J. Fluid. Mech.,* **33,** 639–656.

Turton, J. D., and S. Nicholls, 1987: A study of the diurnal variation of stratocumulus using a multiple mixed layer model. *Quart. J. Roy. Meteor. Soc.,* **113,** 969–1009.

Wakefield, J. S., and W. H. Schubert, 1981: Mixed-layer model simulation of eastern North Pacific stratocumulus. *Mon. Wea. Rev.,* **109,** 1952–1968.

Wang, Q., and D. H. Lenschow, 1995: An observational study of the role of penetrating cumulus in a marine stratocumulus-topped boundary layer. *J. Atmos. Sci.,* **52,** 2778–2787.

Wang, S., 1993: Modeling marine boundary-layer clouds with a two-layer model: A one-dimensional simulation. *J. Atmos. Sci.,* **50,** 4001–4021.

Warren, S. G., C. J. Hahn, J. London, R. M. Chervin, and R. L. Jenne, 1988: Global distribution of total cloud cover and cloud type amounts over ocean. NCAR Tech. Note NCAR/TN-317+STR, National Center for Atmospheric Research, Boulder, CO, 42 pp + 170 plates. [Available from NCAR, P.O. Box 3000, Boulder, CO 80307.]